Advancing Regional Ecosystem Fisheries Overviews with Climate and Environmental Indicators to Enhance Fisheries Management Advice in the Indian Ocean Tuna Commission

Aron, Ranjanee[1]; Marsac, Francis[2]; Murua, Hilario[3]; Andonegi, Eider[4]; Juan-Jordá, Maria José[1]

[1]Instituto Español de Oceanografia (IEO-CSIC), Spain
[2]Institut de Recherche pour le Développement (IRD), France
[3]International Seafood Sustainability Foundation (ISSF), United States
[4]AZTI, Spain

Abstract

Tropical tuna fisheries in the Indian Ocean are central to food security, livelihoods, and economies, yet their dynamics are increasingly influenced by climate and environmental variability. To support the operationalization of the Ecosystem Approach to Fisheries Management (EAFM) within the Indian Ocean Tuna Commission (IOTC), this study analyzes key physical and biochemical indicators that are known to influence ecological processes of tropical tuna species - skipjack (*Katsuwonus pelamis*), yellowfin (*Thunnus albacares*), and bigeye tuna (*Thunnus obesus*). We examine long-term trends and variability in a set of physical and biochemical indicators in two candidate IOTC ecoregions, the Indian Ocean Monsoon Gyre Ecoregion (IOMGE) and the Somali Current Ecoregion (SCE). The results reveal significant spatial and temporal heterogeneity both within and between ecoregions, highlighting the importance of monitoring region-specific environmental indicators to capture differential trends and responses of ecological processes of tuna species. Building on these findings, the study provides a preliminary 'Environment and Climate Change Effects' section of regional Ecosystem Fishery Overviews (EFOs) for the two selected ecoregions, providing an initial framework for integrating climate-informed considerations into fisheries management advice in IOTC.

1. Introduction

The Indian Ocean is a vital region for tuna fisheries that support both global markets and coastal communities (Tidd et al., 2025). The Indian Ocean Tuna Commission (IOTC) is responsible for the

conservation and sustainable use of tuna and tuna-like species in the Indian Ocean (Kambona & Marashi, 1996). Its warm tropical waters provide optimal habitats for the three tropical tuna species - skipjack (*Katsuwonus pelamis*) (SKJ), yellowfin (*Thunnus albacares*) (YFT), and bigeye tuna (*Thunnus obesus*) (BET) (Fonteneau, 1997). Their fisheries are crucial in providing employment, food security, and revenue from commercial trade (Pillai & Satheeshkumar, 2012). However, climate and environmentally driven fluctuations in oceanographic conditions are increasingly influencing the dynamics of tropical tuna populations and their availability to fisheries (Miller, 2007). Numerous studies have documented that changes in oceanographic conditions affect key biological processes in tunas, including distribution, abundance, reproductive conditions, and recruitment success, among others (Lehodey et al., 1997; Kanaji et al., 2012; Erauskin-Extramiana et al., 2019; Dueri et al., 2014). Developing a robust understanding of these complex environmental-ecological interactions is essential for developing adaptive management strategies capable of sustaining tuna populations and the fisheries dependent on them in the face of ongoing climate change (Bahri et al., 2021).

Traditional fisheries management has often relied on single-species advice, with limited consideration of the ecological and environmental context in which these species exist (Howell et al., 2021). The Ecosystem Approach to Fisheries Management (EAFM) offers a framework to move beyond this limitation by explicitly integrating ecological, environmental, and socio-economic considerations into fisheries management advice (Garcia et al., 2003; Howell et al., 2021; Koen-Alonso et al., 2019; ICES 2024a). To operationalize this approach, the IOTC Working Party on Ecosystems and Bycatch (WPEB) has been developing a process to advance the identification of ecologically meaningful regions (ecoregions) within the IOTC convention area, yet large enough to be practical, to be used as a spatial framework to support the development of tools and products for guiding EAFM implementation (Juan-Jordá et al., 2022). Nine candidate ecoregions have been delineated, which aim to provide a spatial framework to support regional collaborative and cross-sectoral ecosystem planning and prioritization, incentivize ecosystem research, and the development of regional integrated ecosystem-based advice products such as Ecocards and Ecosystem Fisheries Overviews (EFOs) to inform fisheries management decisions in IOTC (Rice et al., 2011; ICES, 2020; Zador et al., 2016).

IOTC is currently developing pilot EFOs to synthesise the most relevant ecological, environmental, and fisheries information for selected ecoregions to inform fisheries management decisions (Juan-Jordá et al., 2020). An EFO is considered a science-to-advice product aiming to provide a structured overview of

ecosystem status, environmental variability, and human pressures, among other topics, to support ecosystem-informed fisheries advice (Juan-Jordá et al., 2024). ICES (the International Council for the Exploration of the Sea) pioneered EFOs for European waters, and IOTC WPEB suggested developing pilot EFOs for the Indian Ocean. The sections of an EFO typically cover topics such as climate and environmental indicators, the effect of fisheries on endangered, threatened, and protected (ETP) species, the effect of fisheries on the food web and the state of the food web, the social context in fisheries management, etc. (Fig. 2) (Juan-Jordá et al., 2019). By integrating these diverse aspects, the EFO aims to support ecosystem-based planning, research, and advice for the sustainable management of tuna and tuna-like species.

This study contributes to the development of the 'Environment and Climate Change Effects' section of a pilot EFO by analyzing key environmental and climate indicators in two candidate ecoregions, the Indian Ocean Monsoon Gyre (IOMGE) and Somali Current (SCE), for their relevance for understanding tuna ecology and fisheries dynamics. Specifically, this study identifies, computes, and examines relevant climate, physical, and biochemical indicators to assess their potential effects on the biology and ecology of tropical tuna species. The aim is to support the integration of climate and environmental considerations into IOTC's advisory framework while evaluating the use of ecoregions as spatial units for ecosystem-informed fisheries management advice.

2. Materials & Methods

2.1 Study Area

Two candidate IOTC ecoregions were selected to develop pilot Ecosystem Fisheries Overviews. The IOMGE and SCE were chosen by the IOTC Working Party on Ecosystem and Bycatch (WPEB) as priority ecoregions for developing this science-to-advisory product (IOTC, 2021). To better capture intra-ecoregional environmental variability, both ecoregions were further divided into subregions. The IOMGE was split at 75°E into Western and Eastern subregions since each of the subregions are dominated by different oceanographic processes. The Western region is primarily influenced by the Somali Current system, which includes the Somali coastal upwelling and Oman upwelling systems, whereas the Eastern IOMGE is characterised by a zonal ocean circulation all the way to Indonesia. The SCE was divided at 12°N into Northern and Southern subregions, since the Northern half encompasses the Oman upwelling system, while the Southern region comprises the strong Somali upwelling system

(Fig. 3). Furthermore, to focus on oceanic environmental processes and minimize coastal influences, certain areas were excluded for the development of the environmental indicators. In the IOMGE, waters north of 10°N in the Western subregion and 5°N for the Eastern subregion were excluded to reduce the influence of coastal areas near India and Sri Lanka, as well as the adjacent Arabian Sea and Bay of Bengal. In the SCE, the Red Sea and the Gulf of Persia were excluded because of their predominantly enclosed, coastal oceanographic regimes (Yao et al., 2014; Ibrahim et al., 2020), thereby retaining a representative boundary current system relevant for oceanic tuna ecology.

2.2 Data & Processing

Candidate environmental and climate indicators were examined based on their potential impacts on tropical tuna biology and ecology (Marsac et al., 2024; Marsac, 2017; Stequert & Marsac, 1989; Marsac, 2008; Marsac & LeBlanc, 2000). Six physical and biogeochemical environmental variables and one climate-driven indicator were chosen (Table 1). The six variables were downloaded from publicly available products, accessed through the Copernicus Marine Environment Monitoring System (CMEMS), covering the period 1993 to 2025. Monthly data were utilized to capture the seasonality of the Indian Ocean, including the summer and winter monsoons. Additionally, the Dipole Mode Index was downloaded from the HadISST 8 (Hadley Centre Sea Ice and Sea Surface Temperature) covering the same period.

To evaluate possible collinearity between variables, correlation analyses were conducted prior to calculating the indicators. The Shapiro-Wilk test confirmed normal distribution for sea surface temperature (SST) and dissolved oxygen (DO) at the surface, and Pearson correlation analysis revealed a high negative correlation ($r = -0.88$). Consequently, DO at the surface was excluded from further analysis. Similarly, the relationship between net primary production (NPP) and chlorophyll-a (Chl-a) concentration was evaluated using Pearson ($r=0.988$), Spearman ($\rho=0.994$), and Kendall ($\tau=0.937$) correlation tests due to the slight skew in the NPP data. The high collinearity and the absence of Chl-a model data prior to 1997 led to retaining only NPP for further analysis in both ecoregions.

All data processing and analyses were done using R (version 4.3.1) within RStudio. The packages utilised were, ncdf4 (Pierce, 2025), RNetCDF (Michna & Woods, 2004), dplyr (Wickham et al., 2014a), tidyr (Wickham et al., 2014b), lubridate (Spinu et al., 2010), raster (Hijmans, 2010), terra (Hijmans, 2020), stars (Pebesma, 2018), sf (Pebesma, 2016), ggplot2 (Wickham, 2016), rnaturalearth (Massicotte & South,

2017), cowplot (Wilke, 2015), patchwork (Pedersen, 2019), scales (Wickham et al., 2011), viridis (Garneir, 2015), pracma (Borchers, 2011), zoo (Zeileis et al., 2004).

2.3 Statistical Methods and Indicator Analysis

Gridded monthly data for the region 30°E-120°E, 30°N-30°S, encompassing both IOMGE and SCE, were downloaded and cropped to the spatial boundaries of the ecoregions and their subregions. Units of DO were transformed from mmol/m^3 to mg/L through the conversion equation: mg/L = (mmol/m^3) / 63.8 (ICES, n.d).

Each variable was analyzed across temporal and spatial scales for each ecoregion and subregion (Fig. 3) from January 1993 to March 2025 for physical variables, and until February 2025 for biogeochemical variables. For physical variables, interim monthly data were utilized to fill a six-month gap in data for 2021-2022. Annual temporal anomalies were calculated relative to climatological baselines derived separately for each Copernicus product and applied to the spatial extent of each subregion and ecoregion. For datasets including 1993-2016 years, the baseline was calculated by averaging monthly values within each year and then computing the mean of these yearly averages. Similarly, for datasets including October 2021-October 2024, the same approach was applied over the shorter reference period. Annual anomalies were obtained by subtracting the climatological mean from each year´s values:

- $Anomaly_{year}$ = year - $Baseline_{(1993\text{-}2016)}$
- $Anomaly_{year}$ = year - $Baseline_{(2021\text{-}2024)}$

Spatial analysis included generating monthly maps for each ecoregion and subregions for the most recent complete year (2024) and available months of 2025. Grid-point climatologies were computed for each latitude-longitude cell using the October 2021–October 2024 reference period. Then, spatial anomalies were calculated by subtracting the corresponding monthly climatological mean from observed values: $Anomaly_{i,j,m}$ = $year_{i,j,m}$ - $(2021\text{-}2024)_{i,j,m}$; where i, j, and m are longitude, latitude, and month, respectively. The spatial anomalies for the extreme dipole years were computed using the 1993-2016 baseline owing to their source datasets, modifying the equation as follows: $Anomaly_{i,j,m}$ = $year_{i,j,m}$ - $(1993\text{-}2016)_{i,j,m}$; where i, j, and m, are longitude, latitude, and month respectively.

Additionally, Hovmöller diagrams were used to examine large-scale spatiotemporal patterns, such as seasonal shifts, upwelling events, and IOD episodes in the environmental variables. For the IOMGE, three

latitudinal belts were averaged over latitude and plotted over longitude and time: belt 1 (7°N-3°N), belt 2 (2°N-2°S), and belt 3 (8°S-12°S). For the SCE, the Hovmöller diagrams were averaged over longitude within the two longitudinal belts corresponding to each subregion's range and plotted over latitude and time to capture greater variability along the latitudinal axis.

3. Results

3.1 Climate indicators at the basin scale

The Indian Ocean Dipole phases, defined by the differences in SST anomalies between the western and eastern Indian Ocean, strongly influence regional productivity. Strong positive IOD years, such as 1994, 1998, 2019, 2023, are characterized by warmer SSTs in the western basin, and cooler SSTs in the eastern basin, driving enhanced upwelling and increased nutrient variability in the eastern regions (Fig. 4). In contrast, strong negative IOD events, including 1996, 1999, 2005, 2016, and 2022, display the opposite pattern, with warm anomalies in the east and suppressed productivity.

3.2 Indian Ocean Monsoon Gyre Ecoregion

Physical variables

Sea surface temperature (SST)

The IOMGE has experienced a sustained warming trend over the past three decades, particularly since 2010, with a clear seasonal cycle reflecting the monsoon system (Fig. 5A&B). Spatial patterns of monthly SST over the last 15 months reveal peak temperatures occurring in April & May 2024 in the northern region of IOMGE, followed by a cooling phase during the southwest monsoon (SWM) (Fig. 6). Spatial SST anomalies during 2024 show strong positive deviations, peaking in August & November across the Eastern subregion. This is followed by cooling trends emerging from the Western subregion from December 2024 to March 2025 (Fig. 7).

The negative dipole conditions of December 2024 clearly illustrate how the IOD drives contrasting west-east responses across the two IOMGE subregions (Fig. 8). During a typical extreme positive IOD phase, the Western subregion warms while the Eastern subregion cools due to enhanced upwelling, whereas in a typical negative IOD phase, the pattern reverses, with cooler anomalies in the West and warmer conditions in the East. Isolated warm anomalies also highlight finer-scale spatial heterogeneity.

Latitudinal SST patterns indicate a persistent northward increase in temperature and a stable west-east polarity, with clear signatures of both positive (1997, 2019) and negative dipole (1996, 2016) events (Fig. 9).

Sea surface height (SSH)

SSH trends exhibit an overall increase across the IOMGE, indicating a gradual deepening of the thermocline over time (Fig. 10). Higher SSH values indicate a deeper thermocline, generally associated with reduced nutrient input to surface waters, whereas lower SSH values correspond to shoaling of the thermocline and enhanced nutrient supply. Across the region, SSH is consistently higher in the Eastern subregion, denoting a relatively deeper thermocline compared to the Western subregion (Fig. 10A&B). This west-east polarity is especially pronounced during extreme IOD events. For example, in the strong positive IOD year of 1997, SSH increased in the West (deep thermocline, suppressed productivity) and decreased in the East (shoaled thermocline, increased productivity), while the reverse occurred during the negative IOD of 2016 (Fig. 10C&D).

Spatial patterns of SSH and anomalies over the last 15 months (January-March) reinforce this dipole-driven dynamic, with 2024 reflecting a transition from a weakening positive IOD to a developing negative phase in 2025 (Fig. 11). SSH anomalies shift accordingly, with positive values in the west during 2024 and predominantly negative across the region in 2025, especially in the south, indicating thermocline shoaling and potential productivity enhancement (Fig. 12). In February 2024, SSH anomalies displayed a characteristic positive dipole pattern, with a deeper thermocline in the Western subregion compared to the Eastern (Fig. 13). Conversely, in December 2024, during the negative dipole, SSH was lower in the Western subregion compared to the Eastern, signifying a shoaled thermocline and stronger nutrient inputs in the Western subregion (Fig. 12).

The latitudinal SSH patterns reveal increasing SSH with latitude in both subregions over time, with the Eastern IOMGE maintaining a deeper thermocline across all belts (Fig. 14), particularly evident in Belt 3 (Fig. 14C). The dipole-linked SSH variations are also well reflected in Hovmoller diagrams, which illustrate the temporal evolution of SSH changes across the region.

Biogeochemical variables

Net primary production (NPP)

After a period of decline between 2004 to 2009 in the Western IOMGE and 1997 to 2002 in the Eastern IOMGE, NPP increased sharply from 2021 onward in both subregions. This rise was more pronounced in the Western IOMGE, likely driven by the coastal Somali upwelling system and the open-ocean Seychelles-Chagos Thermocline Ridge (Fig. 15 A&B). Positive IOD years, such as 1997 and 2023, coincide with elevated productivity in the east, whereas negative IOD phases, such as 2005, corresponded to marked declines in productivity (Fig. 15C&D).

Spatial patterns of NPP over the last 14 months reveal high productivity in Western IOMGE during the southwest monsoon, localized peaks around the Maldives island in February 2024, and high equatorial productivity (Fig. 16). Further enhanced upwelling is observed near Indonesia in August 2024 (Fig. 16).

During a typical extreme positive IOD phase, NPP is particularly elevated in the Eastern subregion compared to the Western (Fig. 17). In the Western side of the IOMGE, persistent productivity hotspots, particularly near the equator (Belt 2), suggest localized area-specific biogeochemical responses to oceanographic forces (Fig. 18). Overall, NPP is more sustained and variable in the Western subregion, reflecting strong influence from regional oceanographic features, upwelling processes and monsoonal dynamics.

Dissolved oxygen at 100m depth (DO)

DO concentrations at 100m are consistently higher in the Western IOMGE than in the Eastern, likely reflecting differences in vertical mixing, local productivity and organic matter decomposition processes (Fig. 19). Annual anomalies reveal a strong IOD influence (Fig. 19 C&D): peaks in the Western region during positive dipole years such as 1994, 1997, 2019, and 2023 coincide with low DO values in the Eastern subregion (Fig. 19 C&D), while the opposite occurs during negative dipole years such as 1996, 2005, 2016, and 2022.

Spatial patterns of DO at 100m depth for December 2024 (a negative dipole month) revealed a pronounced west-east polarity, with elevated DO in the Eastern IOMGE, possibly driven by advective transport (Fig. 20). Anomaly maps of DO at 100m highlight this gradient, especially during early 2025, with stronger positive anomalies in the East and a second north-south variation within the region (Fig. 21). Typical peak IOD-related variations are captured in Figure 22, highlighting the December 2024 west-east contrast.

Latitudinal changes over time reinforce the west-east contrast, particularly within Belt 3 (Fig. 23C). With increasing latitude, DO distributions shift: higher concentrations dominate the West at low latitudes, while the East holds higher values at mid-to high-latitudes (Fig. 23A-C).

3.3 Somali Current Ecoregion

Physical variables

Sea surface temperature (SST)

SST in the SCE shows a long-term warming trend across both subregions (Fig. 24A, C, D). Positive IOD years (1997, 2010, 2019, 2023) are consistently associated with SST in both subregions, while negative IOD years (2008, 2016) (Fig. 4) coincide with cooling (Fig. 24). Seasonal dynamics are strongly shaped by monsoon forcing. Spatial patterns of SST show SST cooling along the coasts of Somalia, Yemen, and Oman during the SWM, driven by the dominant coastal Somali upwelling (Fig. 25). During the NEM season, warming increases in the Southern SCE. In contrast, inter-monsoon periods show more spatially uniform patterns.

Localized variability is linked to mesoscale features such as the Great Whirl, which produced a marked SST decrease along the Somali coast in September 2024 (Fig. 26). Additionally the differences between February 2024 (a positive dipole month) and December 2024 (a negative dipole month) clearly displayed the subregional dynamics with lower SSTs during a negative dipole and higher SSTs during a positive one (Fig. 26). Compared to the widespread warm anomalies in the positive IOD year 2024, a cooling trend is observed in the projected negative IOD year of 2025 (Fig. 26). October 1996 and November 1997 characterize typical extreme phases of the IOD with high negative anomalies associated with a negative phase of the IOD and high positive anomalies associated with a positive phase (Fig. 27). These IOD dynamics are clearly captured in the spatio-temporal Hovmöller diagram, which highlights the pronounced SST peaks with the positive dipole year 1998 (Fig. 28).

Sea surface height (SSH)

SSH exhibits an overall increasing trend with a recent decline in both subregions (Fig. 29 A&B). Southern SCE consistently exhibits higher SSH, reflecting a deeper thermocline compared to the Northern SCE. During the positive IOD of 1998, SSH rose sharply in the Southern SCE while remaining stable in the North (Fig. 29 C&D).

Seasonal and spatial variability in SSH is closely tied to monsoon dynamics. Spatial patterns in SSH over the last 15 months show greater SSH variability in the North, likely due to mesoscale eddies and vertical column mixing (Fig. 30). The onset of the SWM triggers thermocline shoaling along the coasts of Somalia, Yemen, and Oman which progresses northward (Fig. 31). In contrast, the NEM reinforces the north-south SSH gradient, with deeper thermocline conditions in the South (Fig. 31). Dipole forcing amplifies these patterns: typical positive IOD phases increase SSH anomalies deepening the thermocline in the South, while typical negative phases lead to negative anomalies, shoaling the thermocline (Fig. 32). The latitudinal changes in SSH over time confirm persistent deeper thermocline conditions in the Southern SCE, especially during positive IOD years (Fig. 33). In the absence of strong IOD events, the thermocline deepens toward 10°N before shoaling in the northernmost SCE, where the shallowest thermocline is observed (Fig. 33).

Biogeochemical variables

Net primary production (NPP)

NPP exhibits contrasting long-term dynamics between subregions. In the North, productivity declined from 1999 to 2009, reaching minimum levels, before rebounding sharply from 2021 onwards (Fig. 34A, C). In the South, NPP fell from 1994 to 1997, stabilized, and increased from 2020, though a decline has re-emerged since 2023 (Fig. 34B, D). On average, the Northern SCE maintains slightly higher NPP than the South.

Seasonality is strongly monsoon-driven: productivity peaks during the SWM, initiated in the South and propagating northward, with elevated levels persisting longer in the North (Fig. 35). In contrast, inter-monsoon periods (April-May and October-November) show minimal NPP (Fig. 35). Dipole forcing modulates these seasonal cycles, with a strong negative IOD phase enhancing productivity along the coasts of Yemen, Oman, and Somalia, and a strong positive phase suppressing it (Fig. 36). For example, the strong positive IOD of 1998 corresponded to a marked decline in Southern NPP (Fig. 37), while NPP in the Northern SCE peaked again in 2024.

Dissolved oxygen at 100m depth (DO)

DO concentrations at 100 m reveal a pronounced north–south gradient, with persistently higher values in the Southern SCE (Fig. 38 A&B). In the North, DO rose until 2015 but has since declined steadily, while

in the South, concentrations remained relatively stable (Fig. 38 A&B). Anomalies of DO at 100m confirm the increase in DO from 2003 to 2016 in the Northern SCE, and thereby stabilizing, whereas in Southern SCE, the anomalies in DO show relative stability (Fig. 38C&D). The contrast between regions is likely linked to differences in productivity and organic matter cycling. Higher NPP and subsequent sinking of organic matter decomposition likely contribute to the lower DO at 100m depth in the Northern SCE (Fig. 39). Ocean circulation caused by seasonal monsoon forcing further shapes oxygen dynamics: during the SWM, DO tends to rise in the South and decline in the North, while NEM months enhance vertical mixing and temporarily elevate DO in the North. Anomalies in DO over the last 14 months indicate a temporary increase in DO in the Northern SCE during early 2025 and a peak during the SWM in 2024, though the overall 2024 shows a declining trend (Fig. 40).

IOD-related impacts are visible as during a typical positive dipole year, the Southern SCE displays a higher level of DO as compared with the Northern, whilst during a typical negative dipole year, the intensity of increased DO in the Southern SCE decreases alongside the Northern SCE (Fig. 41). The latitudinal trends of DO over time confirm higher DO at 100m in the Southern SCE, with increases aligned with positive IOD years (Fig. 42).

4. Discussion

This study provides the first integrated assessment of physical and biogeochemical indicators relevant to the ecological processes of tropical tunas in two candidate IOTC ecoregions—the Indian Ocean Monsoon Gyre Ecoregion (IOMGE) and the Somali Coastal Ecoregion (SCE). By characterizing basin-wide climatic indicators and region-specific patterns of temperature, sea surface height, net primary production, and oxygen concentrations, we identified both common trends across the Indian Ocean and regional signatures such as upwelling systems and intense mesoscale activity linked to the Indian Ocean Dipole, monsoon cycle, and regional oceanographic processes. These environmental drivers, under ongoing climate variability and change, are known to directly influence tuna distribution, spawning success, and recruitment potential, with implications for fisheries productivity. The development and routine monitoring of these environmental indicators and their integration into Ecosystem Fishery Overviews (EFOs) provide IOTC with a structured, science-to-advice tool to anticipate risks, support adaptive management, and strengthen implementation of the Ecosystem Approach to Fisheries Management (EAFM).

4.1 Environmental indicators and potential impacts on the ecological processes of tropical tunas

The analysis revealed distinct yet interconnected patterns of physical and biogeochemical variability in the epipelagic environment across the two ecoregions, reflecting the combined influence of basin-wide and regional oceanographic processes. Both ecoregions showed strong seasonal and interannual variability linked to IOD phases and the monsoon cycle, as well as a long-term warming trend and concurrent deepening of the thermocline as indicated by increasing SSH. These conditions are associated with declining DO concentrations in surface waters, consistent with the strong negative correlation between SST and DO.

Despite these shared patterns, each ecoregion displays distinct regional oceanographic and environmental characteristics. The IOMGE is marked by a strong west-east gradient, primarily influenced by IOD phases, whereas the SCE exhibits a strong north-south contrast, primarily shaped by the coastal Somali and Oman upwelling system. These regional disparities are in agreement with previous findings (Vinayachandran et al., 2021; Vousden et al., 2012; Hermes & Reason, 2008; Murtugudde & Busalacchi, 1999) and reinforce the differential response of the oceanic-influenced IOMGE and coastal-influenced SCE to large-scale climatic variability.

NPP patterns further reflect these regional differences across the two ecoregions. In the IOMGE, NPP variability is greatest in the western region, driven by the influence of multiple upwelling systems. In contrast, the SCE exhibits consistently higher productivity in the northern region, with marked seasonal peaks during the SWM, emphasizing the dominant influence of the coastal upwelling system. DO concentrations at 100m also illustrate regional disparities, with higher DO concentrations in the Western IOMGE and Southern SCE, likely linked to reduced organic matter decomposition and possible enhanced ventilation or advective processes in these regions. In contrast, lower DO concentrations in the eastern part of the IOMGE may be influenced by productivity patterns in adjacent areas such as the Bay of Bengal (Madhupratap et al., 2003). In both ecoregions, areas of high surface productivity were associated with lower subsurface oxygen, reinforcing the inverse link between primary production and oxygen availability at depth.

These environmental trends have direct implications for tropical tuna biology and ecology. Long-term warming in both the IOMGE and SCE is likely to expand habitat for warm-water species such as YFT and SKJ (20-30°C) (Nimit et al., 2020; Dueri et al., 2014), while BET distributions remain tightly constrained by

SST, DO, and depth, with optimal conditions around 240-280m and 2-2.99mg/L DO (Song et al., 2008; Hanamoto, 1986). Tuna spatial distributions and Catch-per-Unit-Effort (CPUE) are also sensitive to IOD phases, with positive events reducing NPP and tuna catches in the Western Indian Ocean, shifting fishing effort eastward (Marsac, 2017; Lan et al., 2013; Marsac & LeBlanc, 2000; Menard et al., 2007; Song et al., 2009).

Spawning success is temperature and oxygen-dependent (Wexler et al., 2011). YFT spawning peaks between 26-29°C and gonad maturation requires 150-190mg/L DO, with larval survival declining above 31°C or below 2.2 mg/L DO (Wexler et al., 2011; Marsac, 2017; Shi et al., 2022). Positive IODs may enhance YFT and SKJ spawning conditions in the western IO but also shift spawning grounds (Marsac, 2017). SKJ growth and reproductive indices respond to NPP, SST, DO, and monsoon cycles, with high values during the NEM in productive upwelling regions such as off Somalia and Madagascar (Fonteneau, 2014). In 2024, SST anomalies in the northern IOMGE exceeded larval survival thresholds, suggesting a potential higher larval mortality risk, while the upwelling-driven SCE may offer greater resilience.

Mesoscale eddies and fronts, especially in the Northern SCE and Western IOMGE, may further enhance larval survival by concentrating prey and reducing dispersal. Intermediate eddy kinetic energy (0.01–0.06 m^2/s^2) is associated with higher larval occurrence (Bakun, 2006; Arrizabalaga et al., 2015; Podesta et al., 1993; Royer et al., 2004; Sagarminaga & Arrizabalaga, 2010). SSH anomalies linked to mesoscale features concentrate prey, providing foraging grounds and favorable conditions for survival (Arrizabalaga et al., 2015).

Overall, climate-driven changes in temperature, oxygen, productivity, and mesoscale dynamics directly influence habitat quality, spawning success, and recruitment success of tropical tunas. Systematic monitoring of environmental indicators and embedding their implications into IOTC fisheries management advice is essential to anticipate ecosystem changes and support adaptive, climate-resilient fisheries management (Juan-Jorda et al., 2024). With this intent, the Indian Ocean Digital Atlas (IODA), planned to be developed in 2026 for the IOTC (Marsac et al., 2024), will consist of an efficient tool to monitor environmental changes and assess the possible impacts on tuna fisheries.

4.2 EFO as Ecosystem-Based Advice Products in EAFM Implementation

This study also contributes directly to the development of the ‘Environmental and Climate Change Effects’ section of EFOs for the IOMGE and SCE (Fig. 2) while complementing other EFO sections

currently under development (Juan-Jordá et al., 2024). Following ICES steps in developing ecosystem-based advisory products at the ecoregion level (ICES, 2019; ICES, 2024a; ICES, 2024b), these efforts strengthen IOTC´s EAFM implementation, aligning with international best practices. In comparison, other tuna RFMOs are also calculating and monitoring environmental indicators at varying spatial scales. For instance, the Inter-American Tropical Tuna Commission (IATTC) Ecosystems Considerations report includes an environmental section for the examination and monitoring of the spatio-temporal physical variability in the eastern Pacific; however, it largely focuses on equatorial zones and lacks formal ecoregional classifications (IATTC 2022; IATTC 2023; IATTC 2024). Hence, a work plan to develop formal ecosystem overviews with adequate delineation of ecoregions has been developed (IATTC 2022-2025). Similarly, several environmental indicators are also monitored in the equatorial region within the Western and Central Pacific Fisheries Commission (WCPFC) convention area. There are efforts to integrate climate and environmental variability into ecosystem-level advisory products (WCPFC 2023; WCPFC 2023; SPC-OFP, 2022; Allain et al., 2020). National reports, such as Australia's 'Climate and Ecosystem Status Report' for the Eastern Tuna and Billfish Fishery, demonstrate the value and benefits of region-specific environmental assessments that directly link environmental variability to fisheries productivity (Eastern Tuna & Billfish Fishery 2023; Eastern Tuna & Billfish Fishery 2024). These reports demonstrate that spatially variable oceanographic conditions may directly influence fisheries productivity and catch rates, reinforcing the importance of adopting ecoregion-based approaches when developing ecosystem-informed management advice.

4.3 Future Directions

This study represents the first attempt at developing the 'Environmental and Climate Change Effects' section of the EFO for the IOMGE and SCE in the IOTC. Several improvements are recommended for consideration in future work to enhance the robustness of the environmental section of the regional EFO science-to-advice products.

Some refining in the calculation of the current selected environmental indicators is needed to address inconsistencies across datasets. In particular, the inconsistency of 0.2m mismatch in depth levels between biogeochemical datasets (the 'Global Ocean Biogeochemistry Hindcast' and 'Global Ocean Biogeochemistry Analysis and Forecast' products) may introduce potentially depth-related biases. Interpolating values to a common depth level would help standardize the datasets and improve comparability of the derived indicators.

Enhancing the robustness and ecological relevance of the selected environmental indicators requires both validation with complementary data sources and refinement of spatial boundaries. Integrating additional data sources such as satellite-derived observations of Chla-a or sea level anomaly (SLA) would strengthen confidence in the observed trends and provide cross-validation for the model-derived outputs. Moreover, initial results from the NPP indicator analysis revealed that elevated productivity near Sri Lanka was primarily driven by coastal effects, leading to an adjustment of the Eastern IOMGE boundary from 10°N to 5°N. Hence, monitoring environmental indicators can provide insights into further sub-classification of regions and future refinements of candidate IOTC ecoregions.

Future efforts could also further select and calculate additional environmental indicators to capture broader ecosystem dimensions and environmental drivers beyond the current suite of indicators. Indicators reflecting variability in salinity, eddy kinetic energy, current intensity, ocean deoxygenation, mixed-layer depth, and thermal stress events (e.g., marine heatwaves), among others, could complement the current physical and biological indicators, thereby providing a more holistic understanding of ecosystem responses. Expanding this work to cover other candidate ecoregions within the IOTC area would additionally enhance the representativeness and comparability of EFO products across the basin, ultimately supporting the development of a consistent and scalable framework for incorporating environmental and climate change considerations into fisheries management advice.

Beyond environmental monitoring to anticipate ecosystem changes, future work should build on quantitatively linking specific environmental indicators to key ecological processes, including tuna physiology, distribution, and life history. Establishing these relationships would enable the explicit incorporation of environmental drivers into population dynamics models, fisheries stock assessments, and management strategy evaluation (MSE) frameworks. Embedding such links into assessment and MSE processes is particularly relevant for tuna RFMOs, as it would allow testing the robustness of management procedures under scenarios of climate and ecosystem variability.

5. Conclusion

By establishing environmental indicators for two candidate ecoregions, this study provides the foundation of the ‘Environmental and Climate Change Effects’ section of EFOs in IOTC. These indicators—including temperature, SSH, productivity, and oxygen—capture key processes that shape tuna

distribution, spawning, and productivity. Incorporating them into fish stock assessment and MSE processes is particularly relevant for tuna RFMOs. This approach would not only improve our capacity to anticipate shifts in stock distribution and productivity but also provide managers with adaptive, climate-informed advice that strengthens the resilience of fisheries and dependent communities.

References

1. Allain, V., Macdonald, J., Nicol, S., Phillips, J. S., & Vourey, E. (2020, August 11–20). *Ecosystem and climate indicators for consideration within the WCPO* (WCPFC-SC16-2020/EB-IP-07). Paper presented at the Scientific Committee, 16th Regular Session (Electronic Meeting). Pacific Community (SPC), Ocean Fisheries Programme (OFP), Noumea, New Caledonia.
2. Arrizabalaga, H., Dufour, F., Kell, L., Merino, G., Ibaibarriaga, L., Chust, G., Irigoien, X., Santiago, J., Murua, H., Fraile, I., Chifflet, M., Goikoetxea, N., Sagarminaga, Y., Aumont, O., Bopp, L., Herrera, M., & Fromentin, J. M. (2015). Global habitat preferences of commercially valuable tuna. *Deep Sea Research Part II: Topical Studies in Oceanography, 113,* 102–112. https://doi.org/10.1016/j.dsr2.2014.07.001
3. Australian Fisheries Management Authority. (2023, June). *Eastern Tuna and Billfish Fishery—Climate and ecosystem status report*. https://www.afma.gov.au/sites/default/files/2025-02/easterntunabf-ce-report-june-2023.pdf
4. Australian Fisheries Management Authority. (2024, June). *Eastern Tuna and Billfish Fishery—Climate and ecosystem status report*. https://www.afma.gov.au/sites/default/files/2024-10/eastern-tuna-and-billfish-fishery-climate-and-ecosystem-status-report-june-2024.pdf
5. Bahri, T., Vasconcellos, M., Welch, D. J., Johnson, J., Perry, R. I., Ma, X., & Sharma, R. (Eds.). (2021). *Adaptive management of fisheries in response to climate change* (FAO Fisheries and Aquaculture Technical Paper No. 667, Vol. 667). Food and Agriculture Organization of the United Nations.
6. Bakun, A. (2006). Fronts and eddies as key structures in the habitat of marine fish larvae: Opportunity, adaptive response and competitive advantage. *Scientia Marina, 70*(S2), 105–122. https://doi.org/10.3989/scimar.2006.70s2105
7. Borchers, H. W. (2011). *pracma: Practical numerical math functions* (Version 2.4.4) [R package]. CRAN. https://doi.org/10.32614/CRAN.package.pracma

8. Dueri, S., Bopp, L., & Maury, O. (2014). Projecting the impacts of climate change on skipjack tuna abundance and spatial distribution. *Global Change Biology, 20*(3), 742–753. https://doi.org/10.1111/gcb.12460
9. Erauskin-Extramiana, M., Arrizabalaga, H., Hobday, A. J., Cabré, A., Ibaibarriaga, L., Arregui, I., Murua, H., Chust, G., & Lehodey, P. (2019). Large-scale distribution of tuna species in a warming ocean. *Global Change Biology, 25*(6), 2043–2060. https://doi.org/10.1111/gcb.14630
10. Fonteneau, A. (1997). *Atlas of tropical tuna fisheries: World catches and environment.* Food and Agriculture Organization of the United Nations.
11. Fonteneau, A. (2014). On the movements and stock structure of skipjack (*Katsuwonus pelamis*) in the Indian Ocean. *Document IOTC TTWG.*
12. García, S. M., Zerbi, A., Aliaume, C., Do Chi, T., & Lasserre, G. (2003). *The ecosystem approach to fisheries: Issues, terminology, principles, institutional foundations, implementation and outlook* (FAO Fisheries Technical Paper No. 443). Food and Agriculture Organization of the United Nations.
13. Garnier, S. (2015). *viridis: Colorblind-friendly color maps for R* (Version 0.6.5) [R package]. CRAN. https://doi.org/10.32614/CRAN.package.viridis
14. Gopalakrishna Pillai, N., & Satheeshkumar, P. (2012). Biology, fishery, conservation and management of Indian Ocean tuna fisheries. *Ocean Science Journal, 47*(4), 411–433. https://doi.org/10.1007/s12601-012-0038-y
15. Hanamoto, E. (1986). Effect of oceanographic environment on bigeye tuna distribution. *Special Report of the Kanagawa Prefectural Fishery Experimental Station, 2,* 1–61.
16. Hermes, J. C., & Reason, C. J. C. (2008). Annual cycle of the South Indian Ocean (Seychelles-Chagos) thermocline ridge in a regional ocean model. *Journal of Geophysical Research: Oceans, 113*(C4), C04035. https://doi.org/10.1029/2007JC004363
17. Hijmans, R. J. (2010). *raster: Geographic data analysis and modeling* (Version 3.6-32) [R package]. CRAN. https://doi.org/10.32614/CRAN.package.raster
18. Hijmans, R. J. (2020). *terra: Spatial data analysis* (Version 1.8-50) [R package]. CRAN. https://doi.org/10.32614/CRAN.package.terra
19. Howell, D., Bentley, N., Fay, G., Hutton, T., Oliveros-Ramos, R., & Kell, L. T. (2021). Combining ecosystem and single-species modeling to provide ecosystem-based fisheries management advice within current management systems. *Frontiers in Marine Science, 7,* 607831. https://doi.org/10.3389/fmars.2020.607831

20. Ibrahim, H. D., Xue, P., & Eltahir, E. A. B. (2020). Multiple salinity equilibria and resilience of Persian/Arabian Gulf basin salinity to brine discharge. *Frontiers in Marine Science, 7,* 573. https://doi.org/10.3389/fmars.2020.00573
21. ICES. (2019). *Celtic Seas Ecoregion – Ecosystem overview.* https://doi.org/10.17895/ICES.ADVICE.5749
22. ICES. (2024a). *Definition and rationale for ICES ecoregions.* General ICES advice guidelines. https://doi.org/10.17895/ICES.ADVICE.23634480.V1
23. ICES. (2024b). *Baltic Sea Ecoregion – Ecosystem overview.* ICES Advice: Ecosystem Overviews. https://doi.org/10.17895/ICES.ADVICE.27256635.V1
24. Inter-American Tropical Tuna Commission, Scientific Advisory Committee. (2022, May 16–20). *Ecosystem considerations* (Document SAC-13-10 Corr.). Paper presented at the 13th Meeting (by videoconference).
25. Inter-American Tropical Tuna Commission, Scientific Advisory Committee. (2023, May 15–19). *Ecosystem considerations* (Document SAC-14-11). Paper presented at the 14th Meeting, La Jolla, California, USA.
26. Inter-American Tropical Tuna Commission, Working Group on Ecosystems and Bycatch. (2024, June 5–6). *Ecosystem considerations* (Document EB-02-01). Paper presented at the 2nd Meeting, La Jolla, California, USA.
27. Inter-American Tropical Tuna Commission. (2022–2025). *Project O.2.d – Develop a workplan for restructuring IATTC's ecosystem considerations into (1) an indicator-based EcoCard and (2) a complementary ecosystem status assessment for the EPO.* Inter-American Tropical Tuna Commission. https://iattc.org/en-us/Research/Project/Detail/O-2-d
28. International Council for the Exploration of the Sea (ICES). (2020). *Definition and rationale for ICES ecoregions.* In *Report of the ICES Advisory Committee, 2020* (ICES Advice 2020, pp. 1–12). https://doi.org/10.17895/ices.advice.6014
29. International Council for the Exploration of the Sea (ICES). (n.d.). *Unit conversions.* ICES. Retrieved August 21, 2025, from https://www.ices.dk/data/tools/Pages/Unit-conversions.aspx
30. Indian Ocean Tuna Commission (IOTC). (2022, September 5–9). *Report of the 18th Session of the IOTC Working Party on Ecosystems and Bycatch Assessment Meeting* (IOTC–2022–WPEB18–R[E], 98 pp.). Online.
31. Juan-Jordá, M., et al. (2019, August 12–20). *Selecting ecosystem indicators for fisheries targeting highly migratory species: An EU project to advance the operationalization of the EAFM in ICCAT*

and IOTC (WCPFC-SC15-2019/EB-WP-12). Paper presented at the Scientific Committee, 15th Regular Session, Pohnpei, Federated States of Micronesia.

32. Juan-Jordá, M.-J., Murua, H., Idárraga-Garcés, V., & Andonegi, E. (2024). *Ecosystem fisheries overviews – Assessing the applicability of IOTC candidate ecoregions as a spatial framework for developing ecosystem-based advisory products* (IOTC-2024-WPEB20(AS)-24, pp. 1–45). Indian Ocean Tuna Commission.
33. Juan-Jordá, M.-J., et al. (2020, July 6–8). *Identification of regions in the IOTC Convention Area to inform the implementation of the ecosystem approach to fisheries management* (IOTC-2020-WPNT10-09, 30 pp.). Paper presented at the WPNT10 – 10th Working Party on Neritic Tunas (Virtual). Indian Ocean Tuna Commission. https://archimer.ifremer.fr/doc/00734/84590/
34. Juan-Jordá, M., Nieblas, A., Tsuji, S., Marsac, F., Chassot, E., Hayes, D., Shahid, U., Khan, M., Andonegi, E., de Bruyn, P., Fiorellato, F., Thoya, P., Green, M., Kitakado, R., Nelson, L., Ramos-Alonso, L., Martin, S., Moss, J., Lopetegui-Eguren, L., … Murua, H. (2022). *Report of the Second IOTC Ecoregion Workshop on "The identification of regions in the IOTC Convention Area to inform the implementation of the ecosystem approach to fisheries management"* (IOTC-2022-WPEB18-22, pp. 1–34). Indian Ocean Tuna Commission.
35. Kanaji, Y., Tanabe, T., Watanabe, H., Oshima, T., & Okazaki, M. (2012). Variability in reproductive investment of skipjack tuna (*Katsuwonus pelamis*) in relation to the ocean–climate dynamics in the tropical eastern Indian Ocean. *Marine and Freshwater Research, 63*(8), 695. https://doi.org/10.1071/MF11146
36. Kambona, J. J., & Marashi, S. H. (1996). *Process for the establishment of the Indian Ocean Tuna Commission* (FAO Fisheries Circular No. 913, 53 pp.). Food and Agriculture Organization of the United Nations.
37. Koen-Alonso, M., Pepin, P., Fogarty, M. J., Kenny, A., & Kenchington, E. (2019). The Northwest Atlantic Fisheries Organization roadmap for the development and implementation of an ecosystem approach to fisheries: Structure, state of development, and challenges. *Marine Policy, 100,* 342–352. https://doi.org/10.1016/j.marpol.2018.11.025
38. Lan, K.-W., Evans, K., & Lee, M.-A. (2013). Effects of climate variability on the distribution and fishing conditions of yellowfin tuna (*Thunnus albacares*) in the western Indian Ocean. *Climatic Change, 119*(1), 63–77. https://doi.org/10.1007/s10584-012-0637-8

39. Lehodey, P., Bertignac, M., Hampton, J., Lewis, A., & Picaut, J. (1997). El Niño Southern Oscillation and tuna in the western Pacific. *Nature, 389*(6652), 715–718. https://doi.org/10.1038/39575
40. Madhupratap, M., Kumar, S. P., Bhattathiri, P. M. A., Kumar, M. D., Raghukumar, S., Nair, K. K. C., & Ramaiah, N. (2003). Biogeochemistry of the Bay of Bengal: Physical, chemical and primary productivity characteristics of the central and western Bay of Bengal during summer monsoon 2001. *Deep Sea Research Part II: Topical Studies in Oceanography, 50*(5), 881–896. https://doi.org/10.1016/S0967-0645(02)00611-2
41. Marsac, F., Gunawardane, N. D. P., & Noel, E. (2024). *An online digital ocean atlas for the Indian Ocean to study the impacts of climate change and variability on tuna fisheries* (IOTC-2024-WPDCS20-27). Indian Ocean Tuna Commission, Working Party on Data Collection and Statistics, 20th Session.
42. Marsac, F. (2008). *Outlook of ocean climate variability in the west tropical Indian Ocean, 1997–2008.* Working document for the Indian Ocean Tuna Commission.
43. Marsac, F. (2017). The Seychelles tuna fishery and climate change. In B. F. Phillips & M. Pérez-Ramírez (Eds.), *Climate change impacts on fisheries and aquaculture* (1st ed., pp. 523–568). Wiley. https://doi.org/10.1002/9781119154051.ch16
44. Marsac, F., & Le Blanc, J. L. (2000). ENSO cycle and purse seine tuna fisheries in the Indian Ocean with emphasis on the 1998–1999 La Niña. *IOTC Proceedings, 3,* 354–363.
45. Massicotte, P., & South, A. (2017). *rnaturalearth: World map data from Natural Earth* (Version 1.0.1) [R package]. CRAN. https://doi.org/10.32614/CRAN.package.rnaturalearth
46. Ménard, F., Marsac, F., Bellier, E., & Cazelles, B. (2007). Climatic oscillations and tuna catch rates in the Indian Ocean: A wavelet approach to time series analysis. *Fisheries Oceanography, 16*(1), 95–104. https://doi.org/10.1111/j.1365-2419.2006.00415.x
47. Michna, P., & Woods, M. (2004). *RNetCDF: Interface to 'NetCDF' datasets* (Version 2.11-1) [R package]. CRAN. https://doi.org/10.32614/CRAN.package.RNetCDF
48. Miller, K. A. (2007). Climate variability and tropical tuna: Management challenges for highly migratory fish stocks. *Marine Policy, 31*(1), 56–70. https://doi.org/10.1016/j.marpol.2006.05.006
49. Murtugudde, R., & Busalacchi, A. J. (1999). Interannual variability of the dynamics and thermodynamics of the tropical Indian Ocean. *Journal of Climate, 12,* 2300–2326. https://doi.org/10.1175/1520-0442(1999)012

50. Nimit, K., Valsala, V., Akiyama, H., Chowdhury, M. R., Singh, P., & Takahashi, K. (2020). Oceanographic preferences of yellowfin tuna (*Thunnus albacares*) in warm stratified oceans: A remote sensing approach. *International Journal of Remote Sensing, 41*(15), 5785–5805. https://doi.org/10.1080/01431161.2019.1707903
51. Pebesma, E. (2016). *sf: Simple features for R* (Version 1.0-21) [R package]. CRAN. https://doi.org/10.32614/CRAN.package.sf
52. Pebesma, E. (2018). *stars: Spatiotemporal arrays, raster and vector data cubes* (Version 0.6-8) [R package]. CRAN. https://doi.org/10.32614/CRAN.package.stars
53. Pedersen, T. L. (2019). *patchwork: The composer of plots* (Version 1.3.0) [R package]. CRAN. https://doi.org/10.32614/CRAN.package.patchwork
54. Pierce, D. (2025, March 25). *ncdf4: Interface to Unidata netCDF (Version 4 or earlier) format data files* [R package]. CRAN. https://cran.r-project.org/web/packages/ncdf4/index.html
55. Podestá, G. P., Browder, J. A., & Hoey, J. J. (1993). Exploring the association between swordfish catch rates and thermal fronts on U.S. longline grounds in the western North Atlantic. *Continental Shelf Research, 13*(2–3), 253–277. https://doi.org/10.1016/0278-4343(93)90109-B
56. Rice, J., Gjerde, K. M., Ardron, J., Arico, S., Cresswell, I., Escobar, E., Grant, S., & Vierros, M. (2011). Policy relevance of biogeographic classification for conservation and management of marine biodiversity beyond national jurisdiction, and the GOODS biogeographic classification. *Ocean & Coastal Management, 54*(2), 110–122. https://doi.org/10.1016/j.ocecoaman.2010.10.010
57. Royer, F., Fromentin, J., & Gaspar, P. (2004). Association between bluefin tuna schools and oceanic features in the western Mediterranean. *Marine Ecology Progress Series, 269,* 249–263. https://doi.org/10.3354/meps269249
58. Sagarminaga, Y., & Arrizabalaga, H. (2010). Spatio-temporal distribution of albacore (*Thunnus alalunga*) catches in the northeastern Atlantic: Relationship with the thermal environment. *Fisheries Oceanography, 19*(2), 121–134. https://doi.org/10.1111/j.1365-2419.2010.00532.x
59. Secretariat. (2023, December 4–8). *Incorporating climate change considerations into conservation and management of WCPO fisheries and ecosystems* (WCPFC20-2023-12). Paper presented at the Twentieth Regular Session, Rarotonga, Cook Islands (Hybrid).
60. Shi, X., Zhang, J., Wang, X., Wang, Y., Li, C., & Shi, J. (2022). Reproductive biology of yellowfin tuna (*Thunnus albacares*) in tropical Western and Central Pacific Ocean. *Fishes, 7*(4), 162. https://doi.org/10.3390/fishes7040162

61. Song, L., Zhou, J., Zhou, Y., Nishida, T., Jiang, W., & Wang, J. (2009). Environmental preferences of bigeye tuna, *Thunnus obesus*, in the Indian Ocean: An application to a longline fishery. *Environmental Biology of Fishes, 85*(2), 153–171. https://doi.org/10.1007/s10641-009-9474-7
62. Song, L. M., Zhang, Y., Xu, L. X., Jiang, W. X., & Wang, J. Q. (2008). Environmental preferences of longlining for yellowfin tuna (*Thunnus albacares*) in the tropical high seas of the Indian Ocean. *Fisheries Oceanography, 17*(4), 239–253. https://doi.org/10.1111/j.1365-2419.2008.00476.x
63. SPC-OFP. (2022, August 10–18). *Ecosystem and climate indicators* (WCPFC-SC18-2022/EB-WP-01). Paper presented at the Scientific Committee, 18th Regular Session, Electronic Meeting.
64. SPC-OFP. (2023, September 20–26). *Ecosystem and climate indicator report card from SC19* (WCPFC-TCC19-2023-IP121). Paper presented at the Technical and Compliance Committee, 19th Regular Session, Pohnpei, Federated States of Micronesia.
65. Spinu, V., Grolemund, G., & Wickham, H. (2010). *lubridate: Make dealing with dates a little easier* (Version 1.9.4) [R package]. CRAN. https://doi.org/10.32614/CRAN.package.lubridate
66. Stéquert, B., & Marsac, F. (1989). *Tropical tuna: Surface fisheries in the Indian Ocean* (No. 282). Food & Agriculture Organization.
67. Tidd, A., Guillotreau, P., Fu, D., Mosqueira, I., Dagorn, L., & Capello, M. (2025). Equitable pathways for sustainable tuna fisheries management in the Indian Ocean. *Marine Policy, 173,* 106563. https://doi.org/10.1016/j.marpol.2024.106563
68. Vinayachandran, P. N. M., et al. (2021). Reviews and syntheses: Physical and biogeochemical processes associated with upwelling in the Indian Ocean. *Biogeosciences, 18*(22), 5967–6029. https://doi.org/10.5194/bg-18-5967-2021
69. Vousden, D., Stapley, J. R., Ngoile, M. A., Sauer, W., & Scott, L. (2012). Climate change and variability of the Agulhas and Somali Current Large Marine Ecosystem in relation to socioeconomics and governance. In *Large marine ecosystems* (Chap. 5, pp. 81–96).
70. Wexler, J. B., Margulies, D., & Scholey, V. P. (2011). Temperature and dissolved oxygen requirements for survival of yellowfin tuna, *Thunnus albacares*, larvae. *Journal of Experimental Marine Biology and Ecology, 404*(1–2), 63–72. https://doi.org/10.1016/j.jembe.2011.04.012
71. Wilke, C. O. (2015). *cowplot: Streamlined plot theme and plot annotations for 'ggplot2'* (Version 1.1.3) [R package]. CRAN. https://doi.org/10.32614/CRAN.package.cowplot
72. Wickham, H. (2016). *ggplot2* (Use R!). Cham, Switzerland: Springer International Publishing. https://doi.org/10.1007/978-3-319-24277-4

73. Wickham, H., François, R., Henry, L., Müller, K., & Vaughan, D. (2014). *dplyr: A grammar of data manipulation* (Version 1.1.4) [R package]. CRAN. https://doi.org/10.32614/CRAN.package.dplyr
74. Wickham, H., Pedersen, T. L., & Seidel, D. (2011). *scales: Scale functions for visualization* (Version 1.4.0) [R package]. CRAN. https://doi.org/10.32614/CRAN.package.scales
75. Wickham, H., Vaughan, D., & Girlich, M. (2014). *tidyr: Tidy messy data* (Version 1.3.1) [R package]. CRAN. https://doi.org/10.32614/CRAN.package.tidyr
76. Yao, F., et al. (2014). Seasonal overturning circulation in the Red Sea: 1. Model validation and summer circulation. *Journal of Geophysical Research: Oceans, 119*(4), 2238–2262. https://doi.org/10.1002/2013JC009004
77. Zador, S., Holsman, K. K., Aydin, K. Y., & Gaichas, S. K. (2016). Ecosystem considerations in Alaska: The value of qualitative assessments. *ICES Journal of Marine Science, 74*(1), 421–430. https://doi.org/10.1093/icesjms/fsw144
78. Zeileis, A., Grothendieck, G., & Ryan, J. A. (2004). *zoo: S3 infrastructure for regular and irregular time series (Z's ordered observations) (Version 1.8-14) [R package]*. CRAN. https://doi.org/10.32614/CRAN.package.zoo

Tables

Table 1. Description of the environmental variables and products used in this study extracted from Copernicus Marine Environment Monitoring System (CMEMS) and Hadley Center, UK.

No.	Variable and Units	Product Name	Product Identifier	Source Provider	Spatial and temporal Resolution	Time Range Used	Depth (m) Used	Access Link
1.	Sea surface temperature (SST) (°C)	Global Ocean Physics Reanalysis	GLOBAL_MULTIYEAR_PHY_001_030	CMEMS	0.083° × 0.083° Monthly	01/01/1993 - 01/06/2021	0.49	https://data.marine.copernicus.eu/product/GLOBAL_MULTIYEAR_PHY_001_030/description

		Global Ocean Physics Reanalysis	GLOBAL_MULTIYEAR_PHY_001_030	CMEMS	0.083° × 0.083° Monthly	01/07/2021-31/05/2022	0.49	https://data.marine.copernicus.eu/product/GLOBAL_MULTIYEAR_PHY_001_030/description
		Global Ocean Physics Analysis and Forecast	GLOBAL_ANALYSISFORECAST_PHY_001_024	CMEMS	0.083° × 0.083° Monthly	01/06/2022-01/03/2025	0.49	https://data.marine.copernicus.eu/product/GLOBAL_ANALYSISFORECAST_PHY_001_024/description
2.	Sea surface height above geoid (SSH) (m)	Global Ocean Physics Reanalysis	GLOBAL_MULTIYEAR_PHY_001_030	CMEMS	0.083° × 0.083° Monthly	01/01/1993 - 01/06/2021	0.49	https://data.marine.copernicus.eu/product/GLOBAL_MULTIYEAR_PHY_001_030/description
		Global Ocean Physics Reanalysis	GLOBAL_MULTIYEAR_PHY_001_030	CMEMS	0.083° × 0.083° Monthly	01/07/2021-31/05/2022	0.49	https://data.marine.copernicus.eu/product/GLOBAL_MULTIYEAR_PHY_001_030/description
		Global Ocean Physics Analysis and Forecast	GLOBAL_ANALYSISFORECAST_PHY_001_024	CMEMS	0.083° × 0.083° Monthly	01/06/2022-01/03/2025	0.49	https://data.marine.copernicus.eu/product/GLOBAL_ANALYSISFORECAST_PHY_001_024/description
3.	Net primary production of biomass	Global Ocean Biogeoc	GLOBAL_MULTIYEAR_BGC_0	CMEMS	0.25° × 0.25° Monthly	01/01/1993 - 01/12/2	0.51	https://data.marine.copernicus.eu/pr

	expressed as carbon per unit volume in sea water (NPP) ($mg/m^3/day$)	hemistry Hindcast	01_029			022		oduct/GLOBAL_MULTIYEAR_BGC_001_029/description
		Global Ocean Biogeochemistry Analysis and Forecast	GLOBAL_ANALYSISFORECAST_BGC_001_028	CMEMS	0.25° × 0.25° Monthly	01/01/2023 - 01/02/2025	0.49	https://data.marine.copernicus.eu/product/GLOBAL_ANALYSISFORECAST_BGC_001_028/description
4.	Mass concentration of chlorophyll a in sea water (CHL) (mg/m^3)	Global Ocean Biogeochemistry Hindcast	GLOBAL_MULTIYEAR_BGC_001_029	CMEMS	0.25° × 0.25° Monthly	01/01/1993 - 01/12/2022	0.51	https://data.marine.copernicus.eu/product/GLOBAL_MULTIYEAR_BGC_001_029/description
		Global Ocean Biogeochemistry Analysis and Forecast	GLOBAL_ANALYSISFORECAST_BGC_001_028	CMEMS	0.25° × 0.25° Monthly	01/01/2023 - 01/02/2025	0.49	https://data.marine.copernicus.eu/product/GLOBAL_ANALYSISFORECAST_BGC_001_028/description
5.	Mole concentration of dissolved molecular oxygen in sea water (DO) ($mmol/m^3$)	Global Ocean Biogeochemistry Hindcast	GLOBAL_MULTIYEAR_BGC_001_029	CMEMS	0.25° × 0.25° Monthly	01/01/1993 - 01/12/2022	0.51	https://data.marine.copernicus.eu/product/GLOBAL_MULTIYEAR_BGC_001_029/description
		Global Ocean Biogeoc	GLOBAL_ANALYSISFORECAS	CMEMS	0.25° × 0.25° Monthly	01/01/2023 - 01/02/2	0.49	https://data.marine.copernicus.eu/pr

		hemistry Analysis and Forecast	T_BGC_001_028			025		oduct/GLOBAL_ANALYSISFORECAST_BGC_001_028/description
6.	Mole concentration of dissolved molecular oxygen in sea water (DO) at 100m (mmol/m^3)	Global Ocean Biogeochemistry Hindcast	GLOBAL_MULTIYEAR_BGC_001_029	CMEMS	0.25° × 0.25° Monthly	01/01/1993 - 01/12/2022	97.04	https://data.marine.copernicus.eu/product/GLOBAL_MULTIYEAR_BGC_001_029/description
		Global Ocean Biogeochemistry Analysis and Forecast	GLOBAL_ANALYSISFORECAST_BGC_001_028	CMEMS	0.25° × 0.25° Monthly	01/01/2023 - 01/02/2025	92.33	https://data.marine.copernicus.eu/product/GLOBAL_ANALYSISFORECAST_BGC_001_028/description
7.	Dipole Mode Index Series (DMI) (°C)	Hadley Centre, UK	HadISST1.1 product	HadISST	- Monthly	01/1993 - 01/2025	-	https://psl.noaa.gov/gcos_wgsp/Timeseries/Data/dmi.had.long.data

Figures

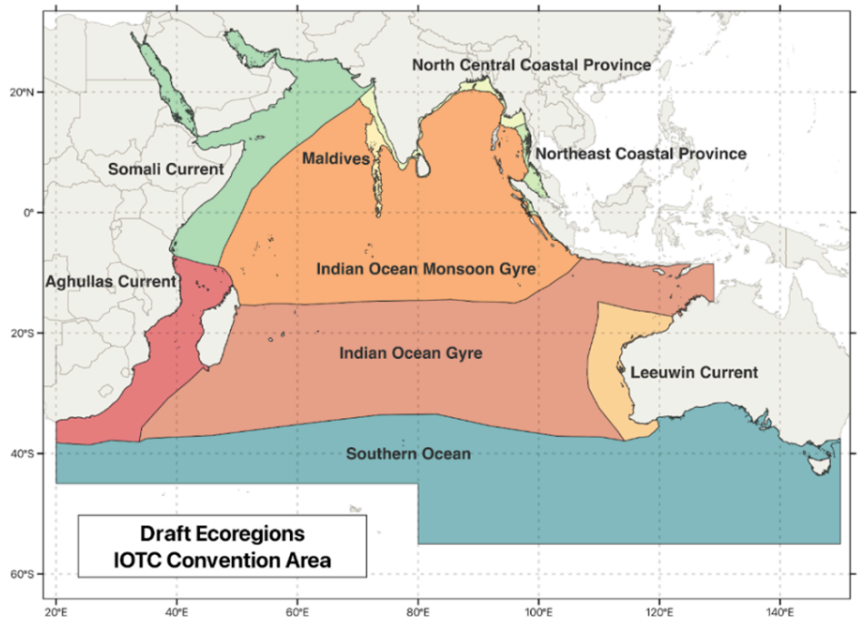

Figure 1. Candidate ecoregions within the IOTC convention area. Spatial units balancing ecological relevance and operational feasibility for promoting regional ecosystem-based planning, scientific research, and the production of tools and advice products to inform fisheries management. Source: Juan-Jorda et al., 2022

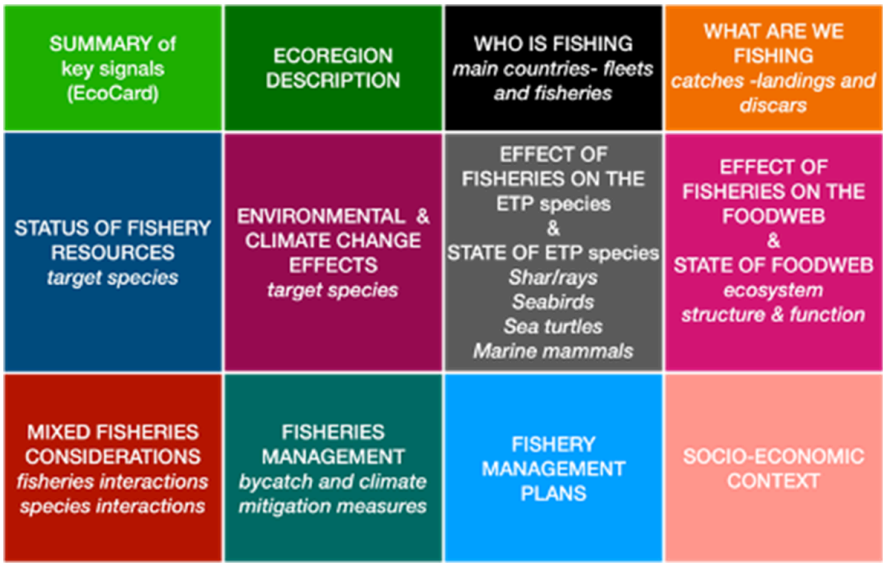

Figure 2. Potential sections of an Ecosystem Fisheries Overview (EFO). Regional EFOs aim to provide a holistic narrative of each ecoregion, focusing on the main species and fisheries under management and their effect on ecosystems. Source: Juan-Jorda et al., 2024

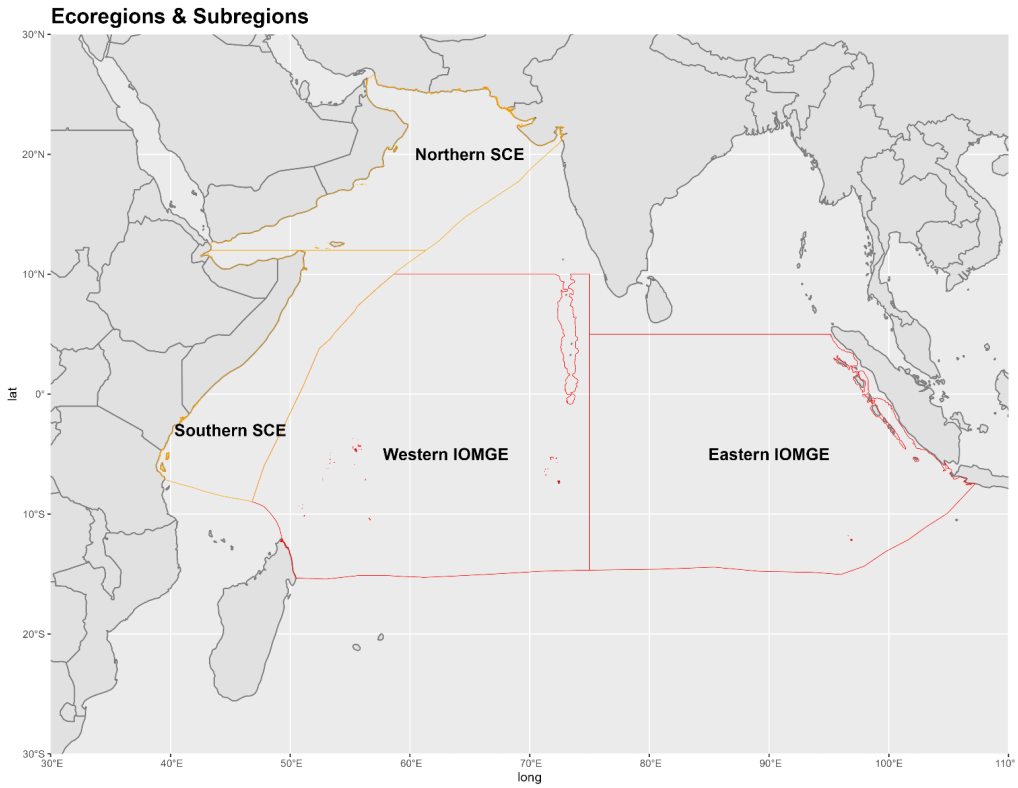

Figure 3. Indian Ocean Monsoon Gyre Ecoregion (IOMGE) and associated subregions, along with Somali Current Ecoregion (SCE) and related subregions.

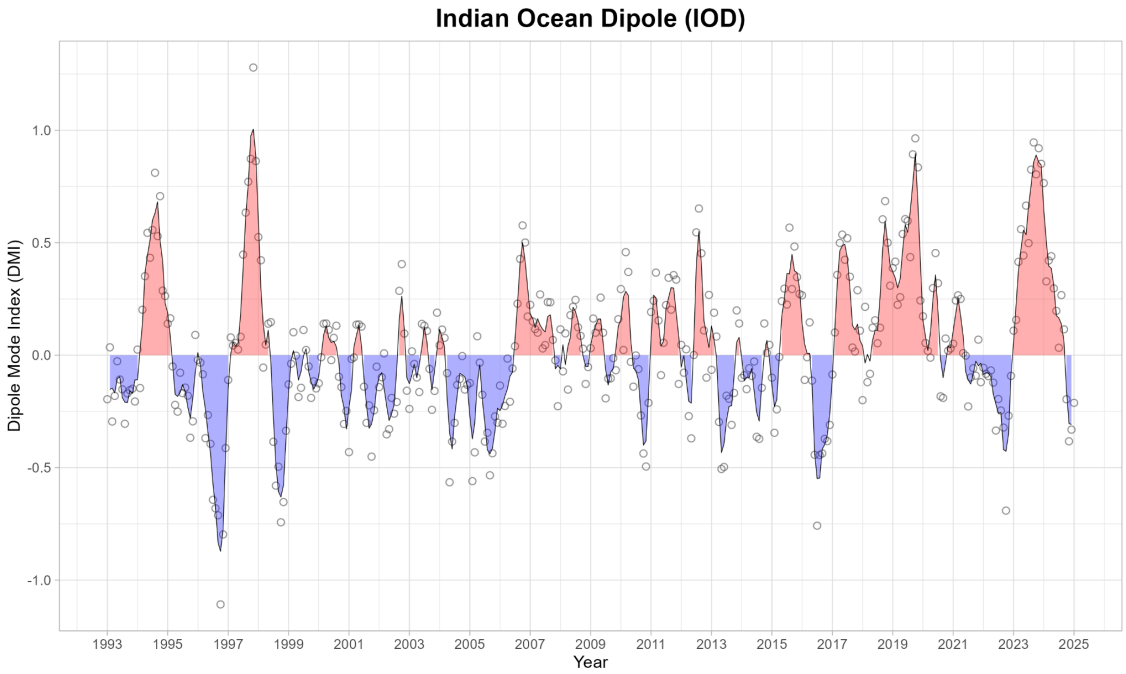

Figure 4. Indian Ocean Dipole Index from January 1993 to January 2025, based on a 3-month centered rolling average. The monthly values are represented by grey circles. Positive anomalies are represented in red and negative anomalies in blue. Source: Hadley Centre, UK (HadISST1.1 product).

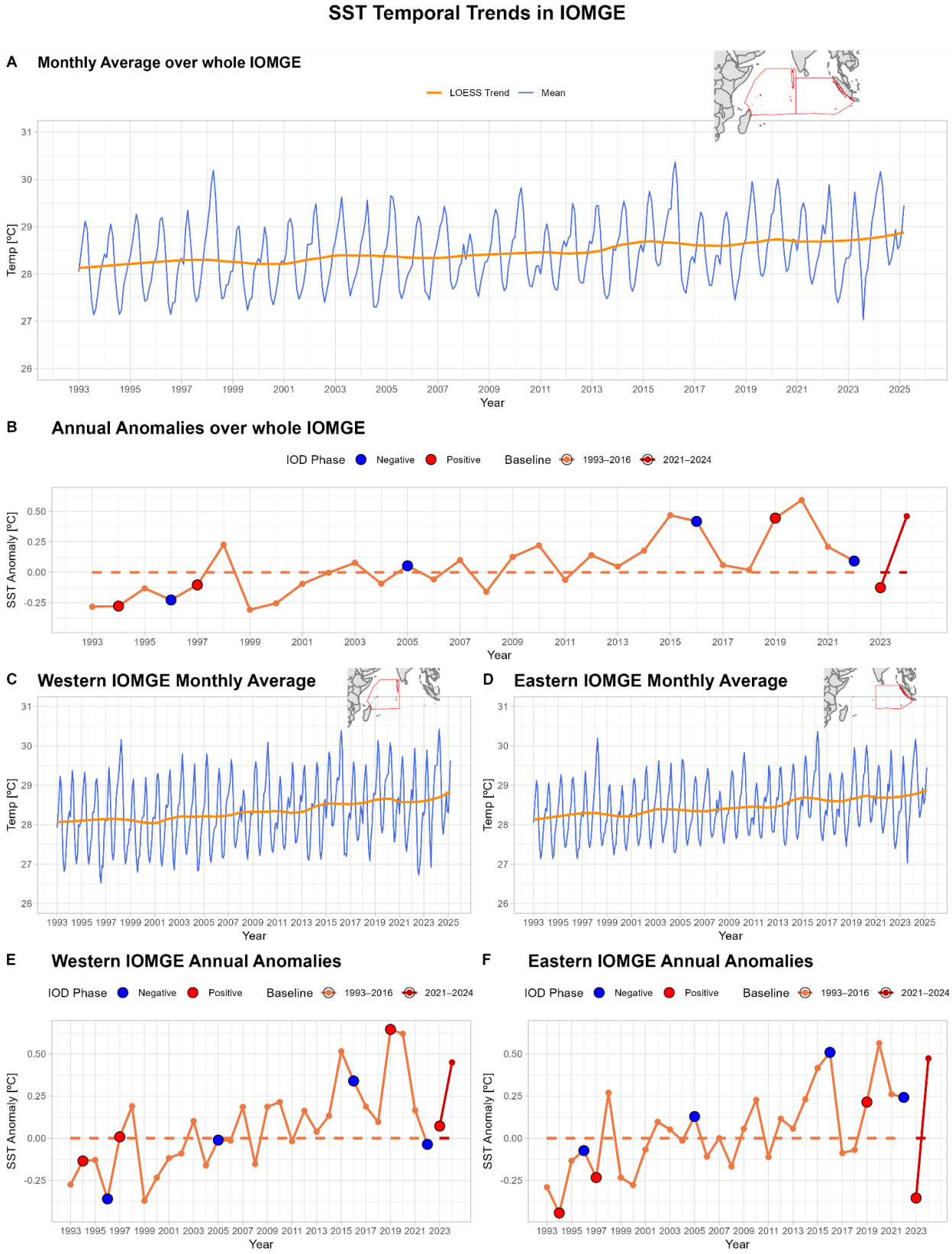
SST Temporal Trends in IOMGE
A Monthly Average over whole IOMGE
LOESS Trend
Mean
Temp [°C]
Year
B Annual Anomalies over whole IOMGE
IOD Phase
Negative
Positive
Baseline
1993–2016
2021–2024
SST Anomaly [°C]
Year
C Western IOMGE Monthly Average
D Eastern IOMGE Monthly Average
E Western IOMGE Annual Anomalies
F Eastern IOMGE Annual Anomalies

Figure 5. Temporal trends of sea surface temperature (SST) and corresponding anomalies across the IOMGE region and its subregions (Western and Eastern IOMGE, divided at 75°E).
A) Monthly mean SST across the entire IOMGE (January 1993–March 2025).
B) Annual SST anomalies across the entire IOMGE, relative to two baselines: 1993–2016 baseline & 2021-2024 baseline. Along with the addition of positive IOD years (red dots) and negative IOD years (blue dots).
C) Monthly mean SST in the Western IOMGE (January 1993-March 2025).
D) Monthly mean SST in the Eastern IOMGE (January 1993-March 2025).
E) Annual SST anomalies in the Western IOMGE till 2024 (baselines: 1993-2016 & 2021-2024). Alongwith the addition of positive IOD years (red dots) and negative IOD years (blue dots).
F) Annual SST anomalies in the Eastern IOMGE till 2024 (baselines: 1993-2016 & 2021-2024). Alongwith the addition of positive IOD years (red dots) and negative IOD years (blue dots).
Note: Data for June 2021 comprises just one date, i.e, 01/06/2021. LOESS trends are shown in orange.

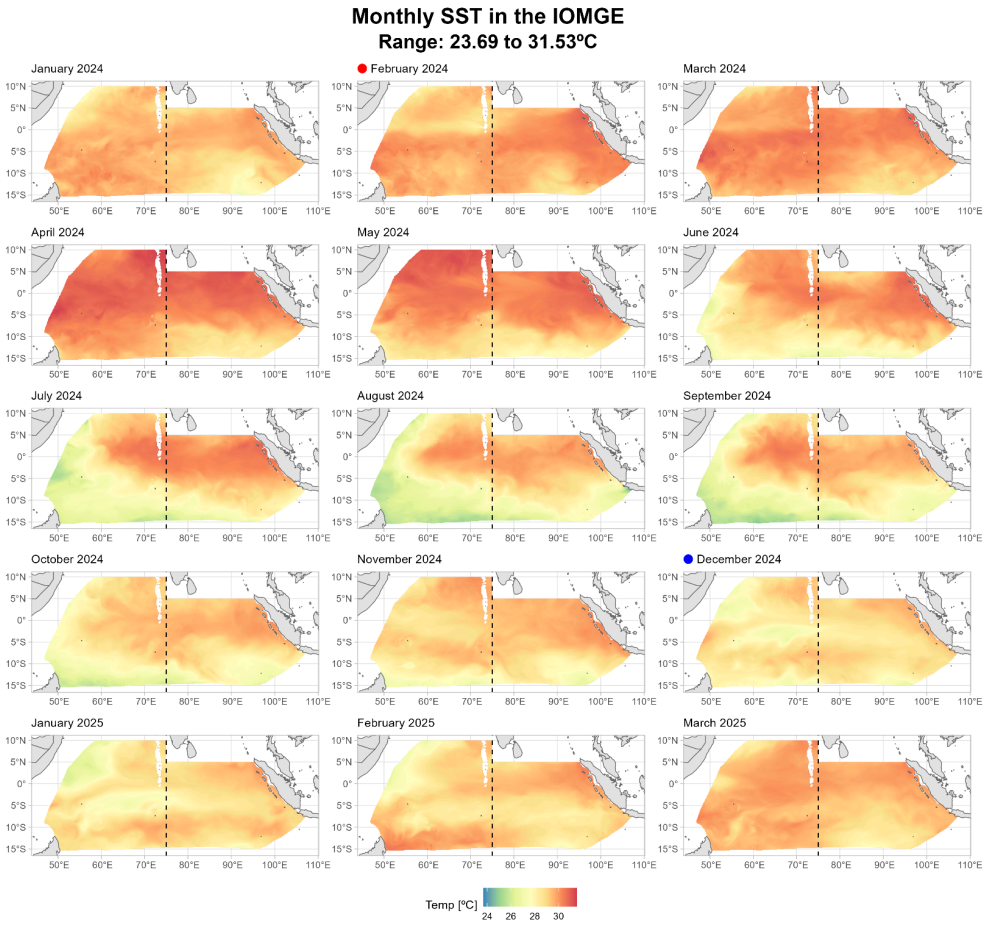

Figure 6. Monthly sea surface temperature (SST) in the IOMGE from January 2024 to March 2025. Dashed black line at 75°E represents the separation between the Western IOMGE and Eastern IOMGE. The red dot represents a positive Indian Ocean Dipole phase and the blue dot represents a negative Indian Ocean Dipole phase.

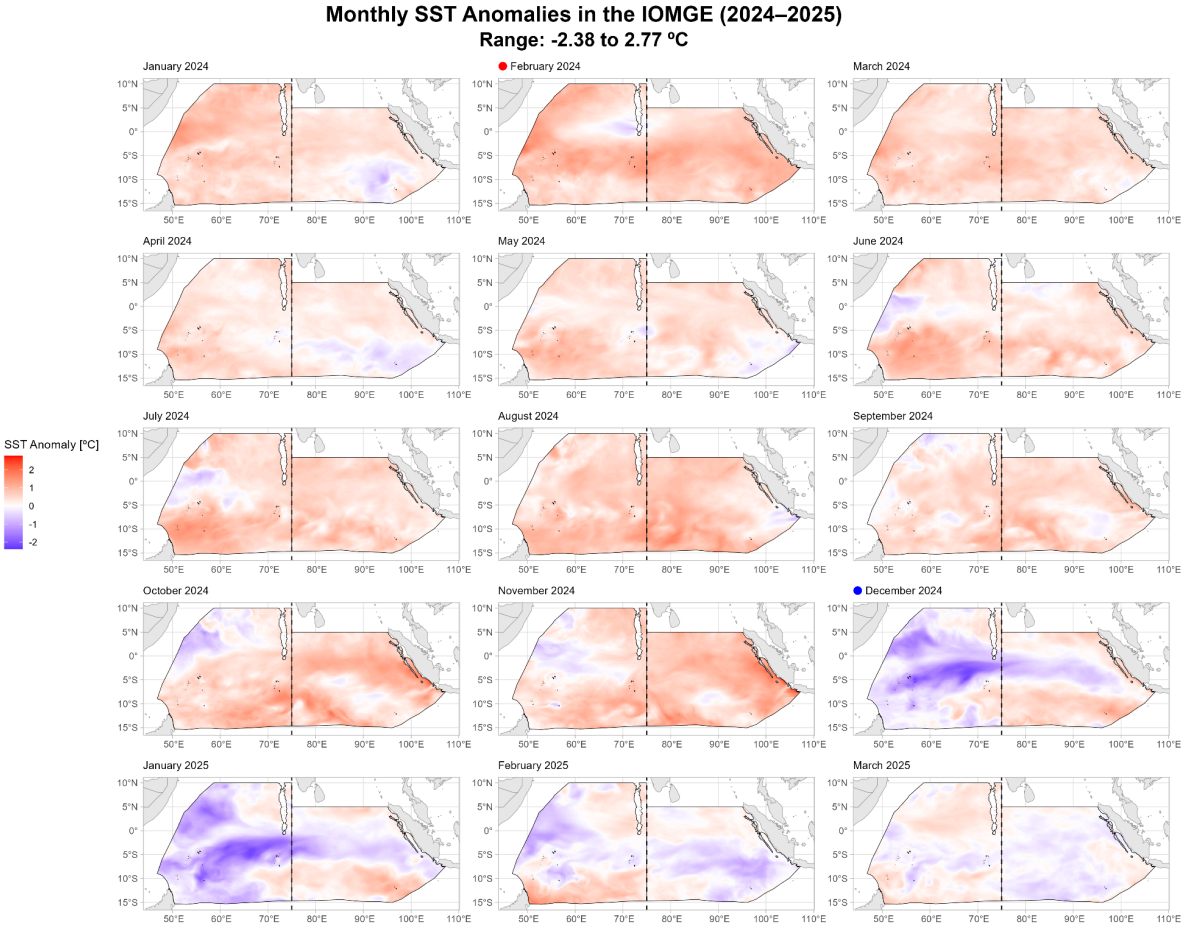

Figure 7. Monthly sea surface temperature (SST) anomalies in the IOMGE from January 2024 to March 2025. Dashed black line at 75°E represents the separation between the Western IOMGE and Eastern IOMGE. The red dot represents a positive Indian Ocean Dipole phase and the blue dot represents a negative Indian Ocean Dipole phase.

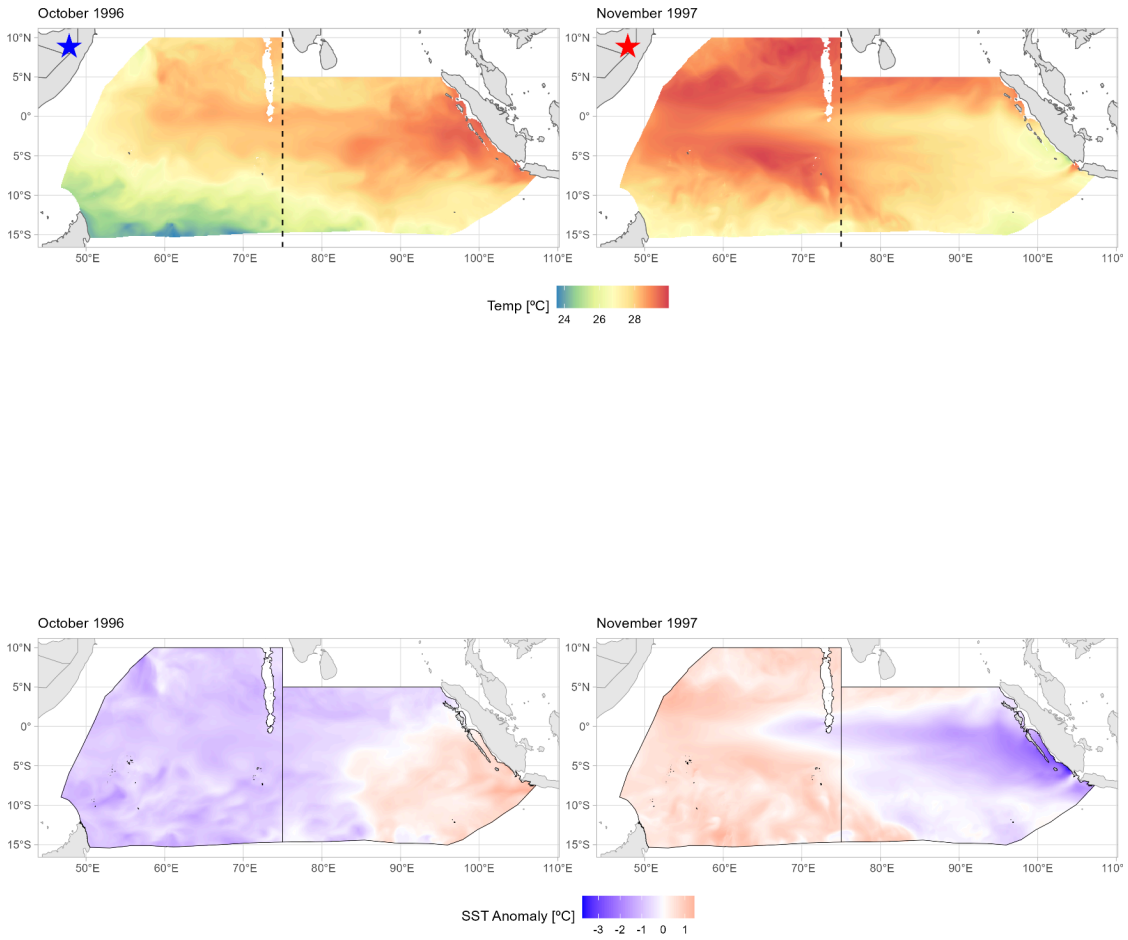

Figure 8. Spatial SST values during extreme negative Indian Ocean Dipole year October 1996 (blue star) and associated anomalies and during extreme positive Indian Ocean Dipole year November 1997 (red star) and assocaited anomalies.

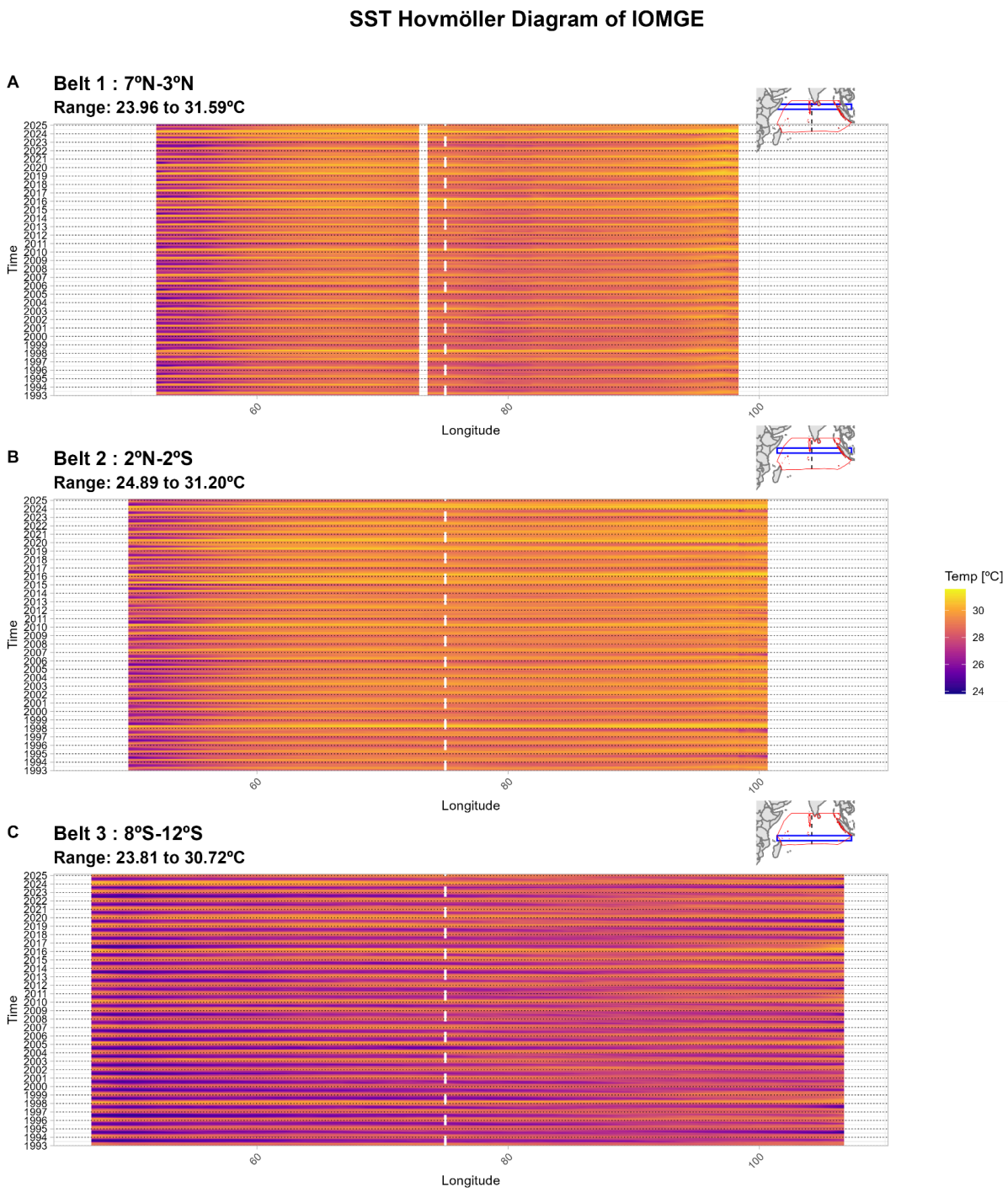

Figure 9. Hovmöller diagrams of monthly sea surface temperature (SST) across three latitudinal belts in the IOMGE from 1993 to 2025. Dashed line represents 75°E separating the Western and Eastern IOMGE.

A) SST values averaged over 7°N-3°N latitudinal range and varying across longitude and time. NA values represented as a gap due to Maldives land data.

B) SST values averaged over 2°N-2°S latitudinal range and varying across longitude and time.

C) SST values averaged over 8°S-12°S latitudinal range and varying across longitude and time.

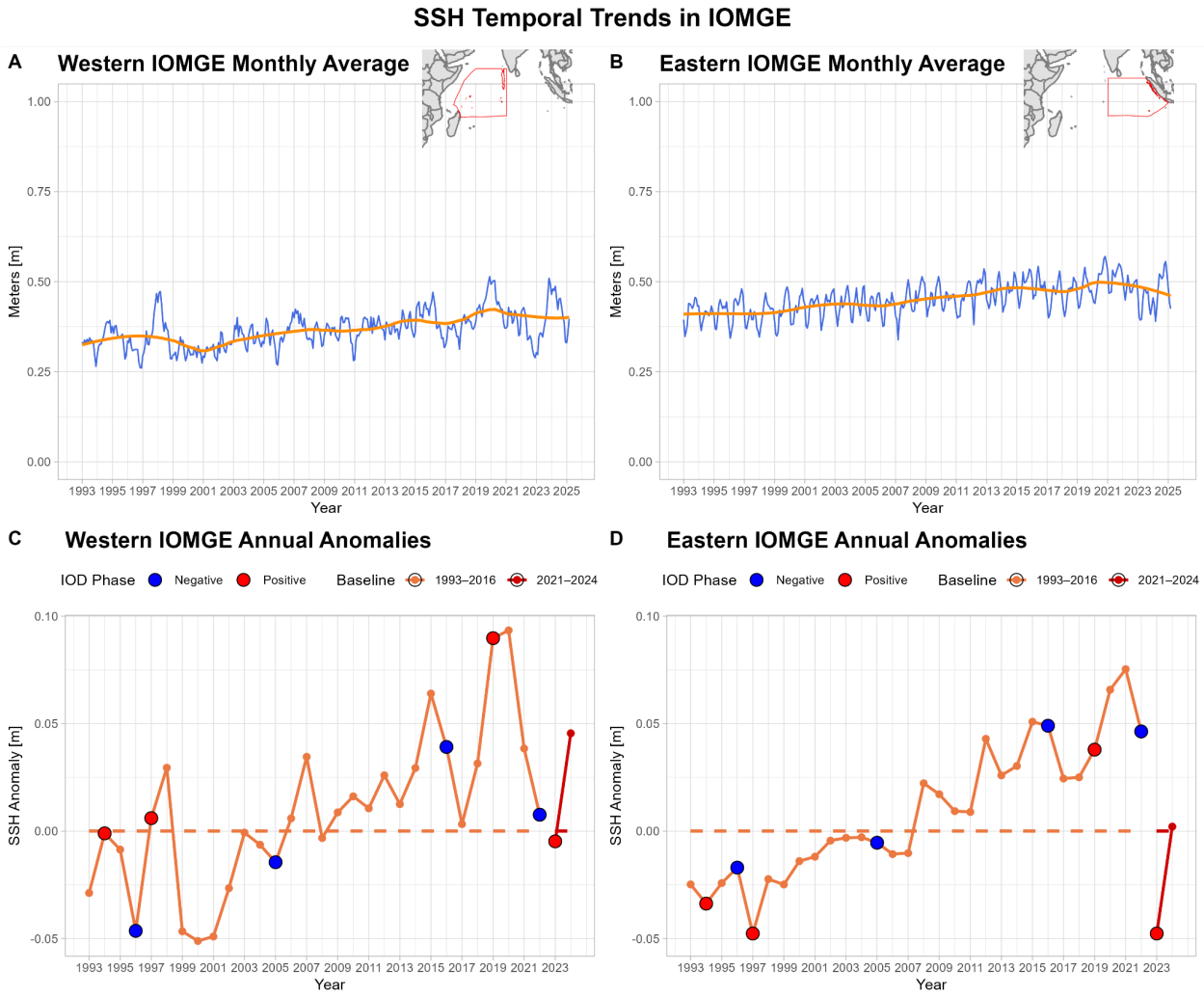

Figure 10. Time series of sea surface height (SSH) and corresponding anomalies across the IOMGE subregions (Western and Eastern IOMGE, divided at 75°E).

A) Monthly mean SSH in the Western IOMGE (January 1993-March 2025).

B) Monthly mean SSH in the Eastern IOMGE (January 1993-March 2025).

C) Annual SSH anomalies in the Western IOMGE till 2024 (baselines: 1993-2016 & 2021-2024). Along with the addition of positive IOD years (red dots) and negative IOD years (blue dots).

D) Annual SSH anomalies in the Eastern IOMGE till 2024 (baselines: 1993-2016 & 2021-2024). Along with the addition of positive IOD years (red dots) and negative IOD years (blue dots).

Note: Data for June 2021 comprises just one date, i.e, 01/06/2021. LOESS trends are shown in orange.

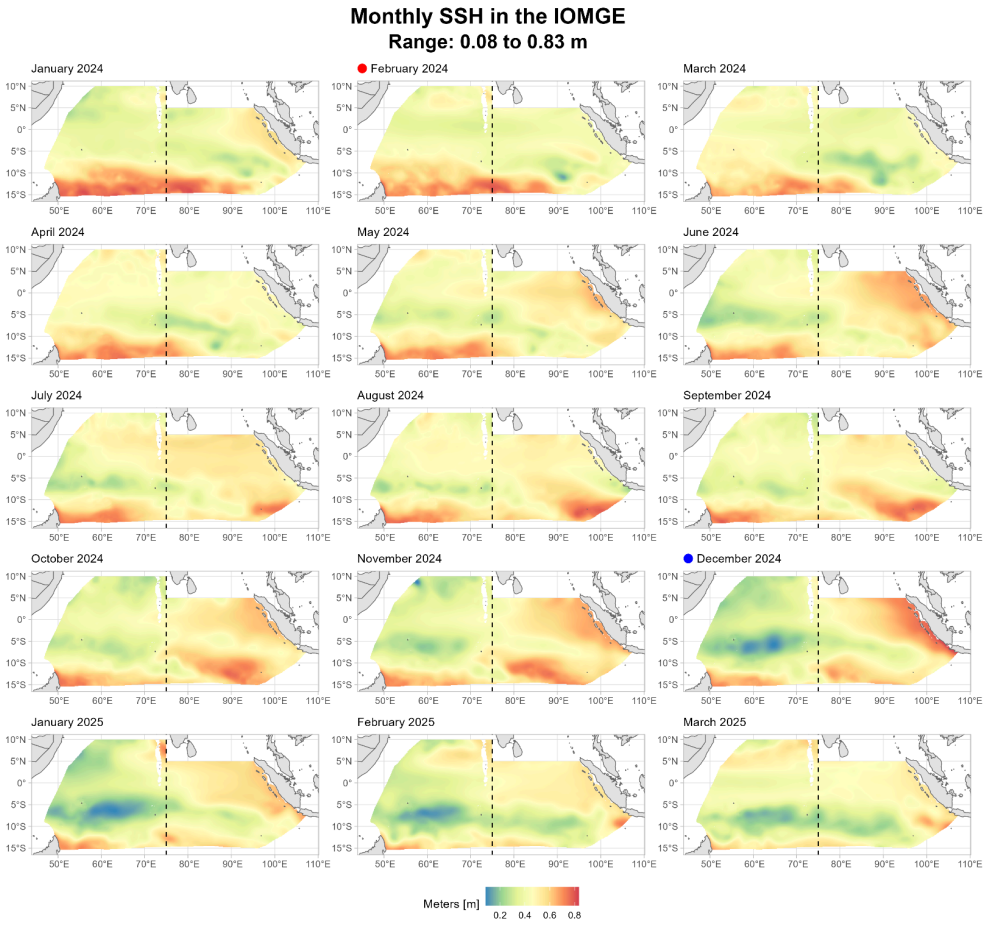

Figure 11. Monthly sea surface height (SSH) in the IOMGE from January 2024 to March 2025. Dashed black line at 75°E represents the separation of the Western IOMGE and Eastern IOMGE. The red dot represents a positive Indian Ocean Dipole phase and the blue dot represents a negative Indian Ocean Dipole phase.

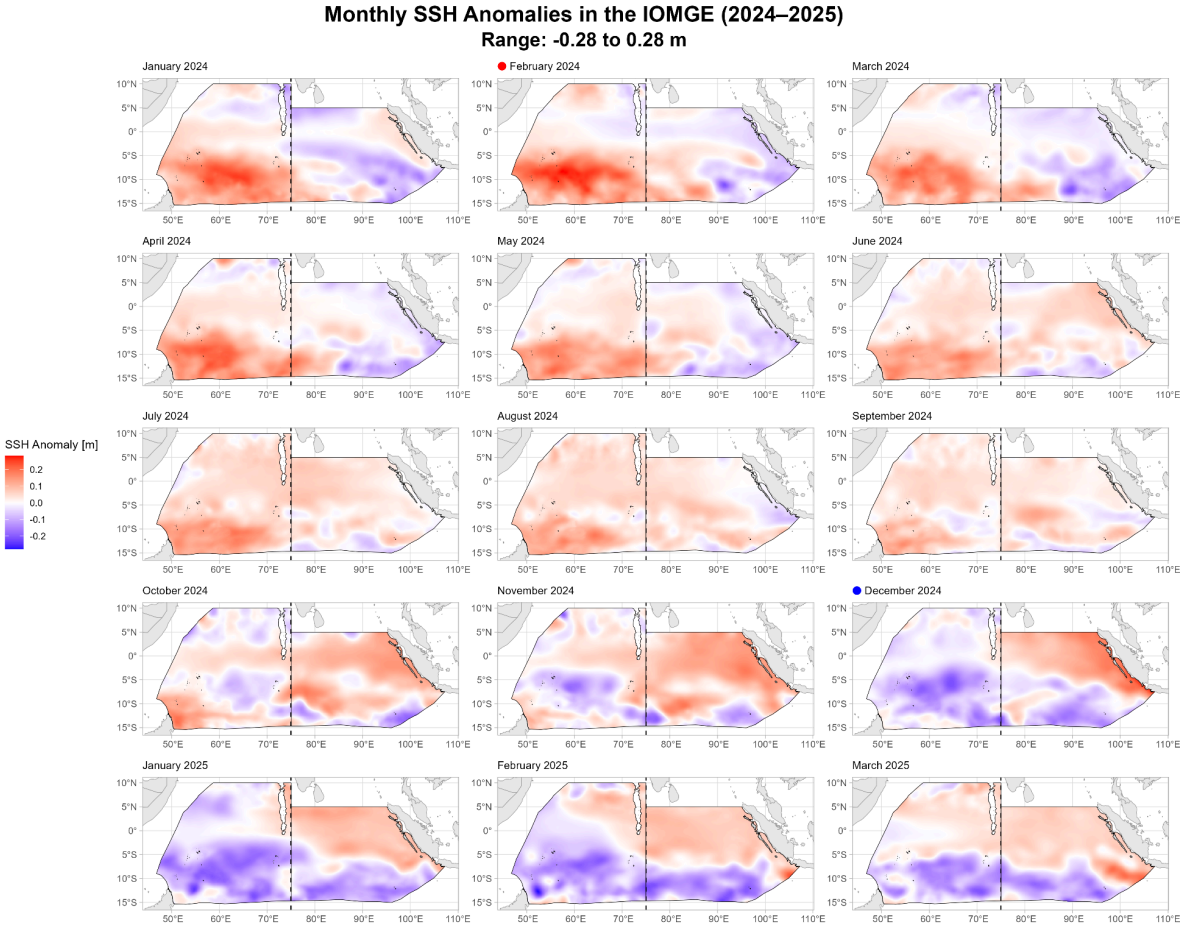

Figure 12. Monthly sea surface height (SSH) anomalies in the IOMGE from January 2024 to March 2025. Dashed black line at 75°E represents the separation of the Western IOMGE and Eastern IOMGE. The red dot represents a positive Indian Ocean Dipole phase and the blue dot represents a negative Indian Ocean Dipole phase.

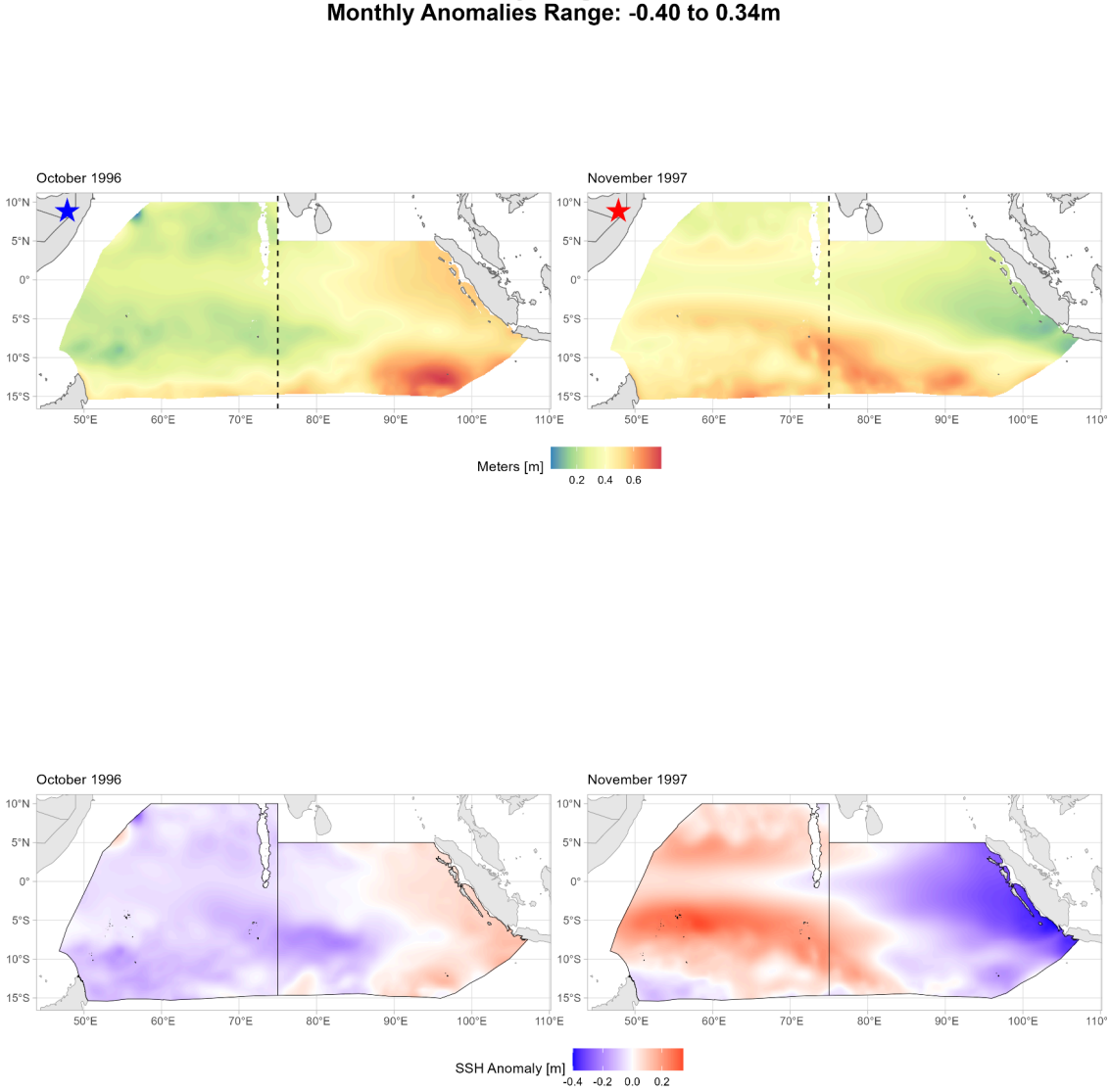

Figure 13. Spatial SSH values during extreme negative Indian Ocean Dipole year October 1996 (blue star) and associated anomalies and during extreme positive Indian Ocean Dipole year November 1997 (red star) and associated anomalies.

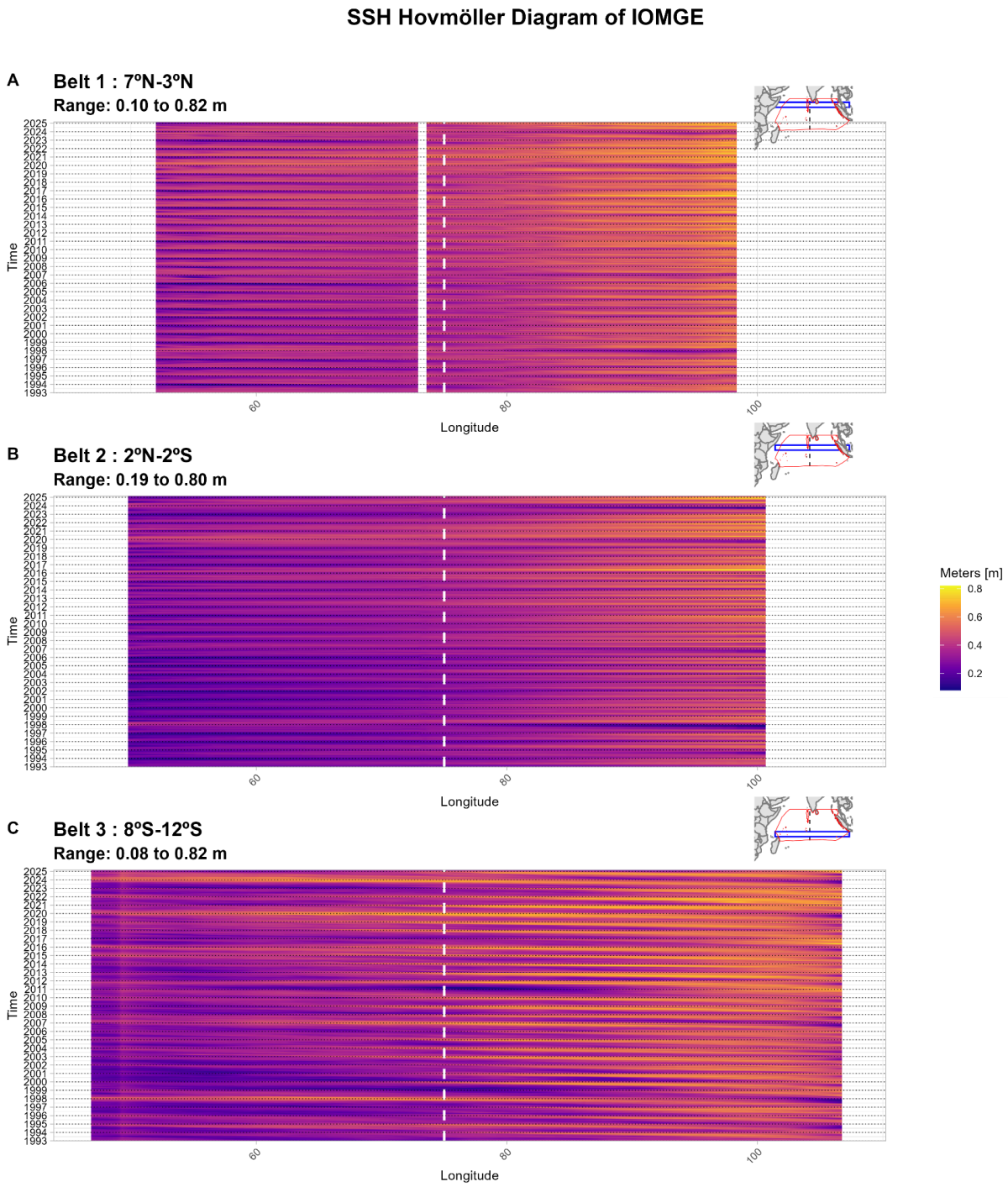

Figure 14. Hovmöller diagrams of monthly sea surface height (SSH) across three latitudinal belts in the IOMGE from 1993 to 2025. Dashed line represents 75°E separating Western and Eastern IOMGE.

A) SSH values averaged over 7°N-3°N latitudinal range and varying across longitude and time. NA values represented as a gap due to Maldives land data.

B)SSH values averaged over 2°N-2°S latitudinal range and varying across longitude and time.

C)SSH values averaged over 8°S-12°S latitudinal range and varying across longitude and time.

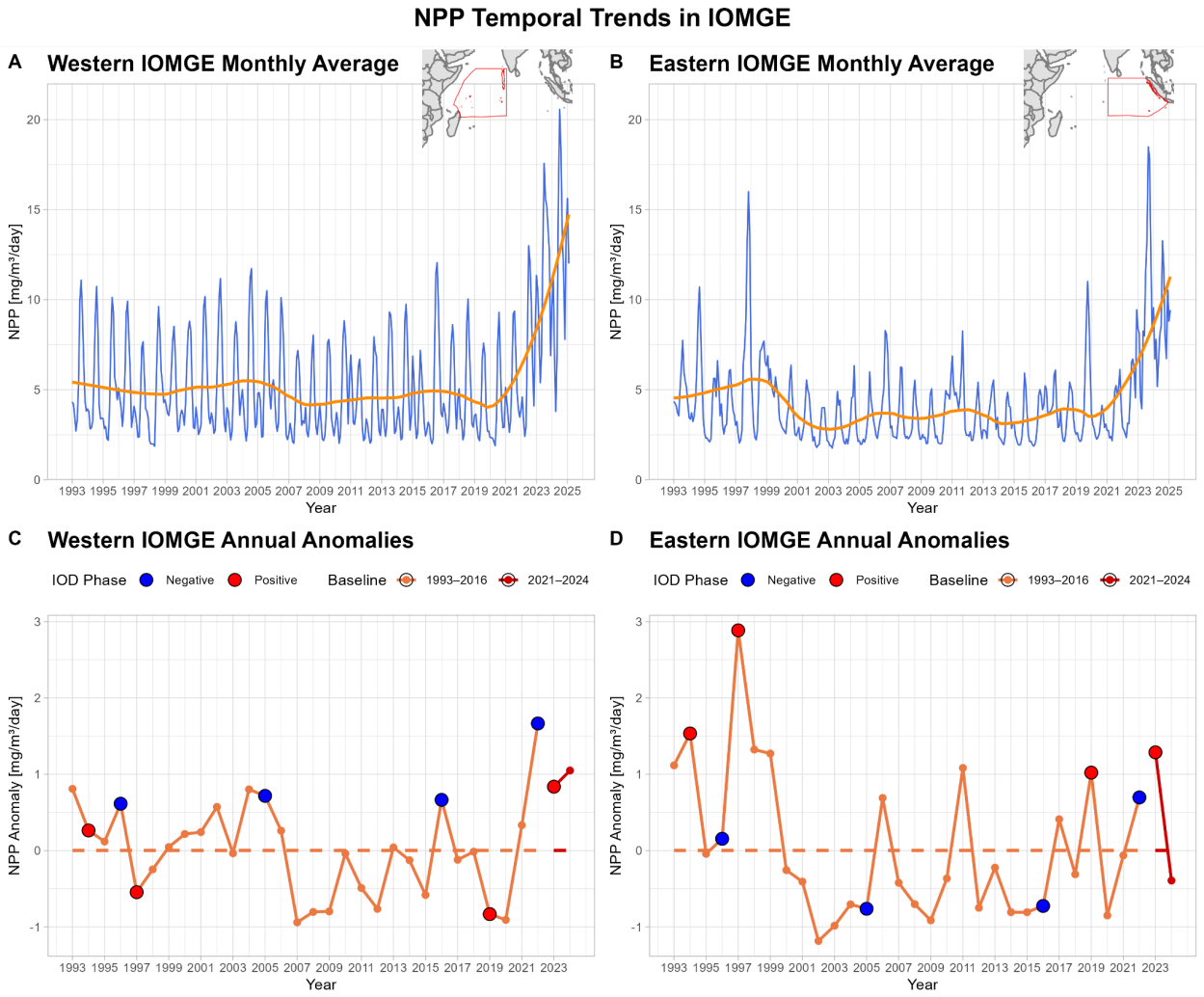

Figure 15. Time series of net primary production (NPP) and corresponding anomalies across the IOMGE subregions (Western and Eastern IOMGE, divided at 75°E).

A) Monthly mean NPP in the Western IOMGE region (January 1993-February 2025).

B) Monthly mean NPP in the Eastern IOMGE region (January 1993-Februray 2025).

C) Annual NPP anomalies in the Western IOMGE region till 2024 (baselines: 1993-2016 & 2021-2024). Along with the addition of positive IOD years (red dots) and negative IOD years (blue dots).

D) Annual NPP anomalies in the Eastern IOMGE region till 2024 (baselines: 1993-2016 & 2021-2024). Along with the addition of positive IOD years (red dots) and negative IOD years (blue dots).

Note: LOESS trends are shown in orange.

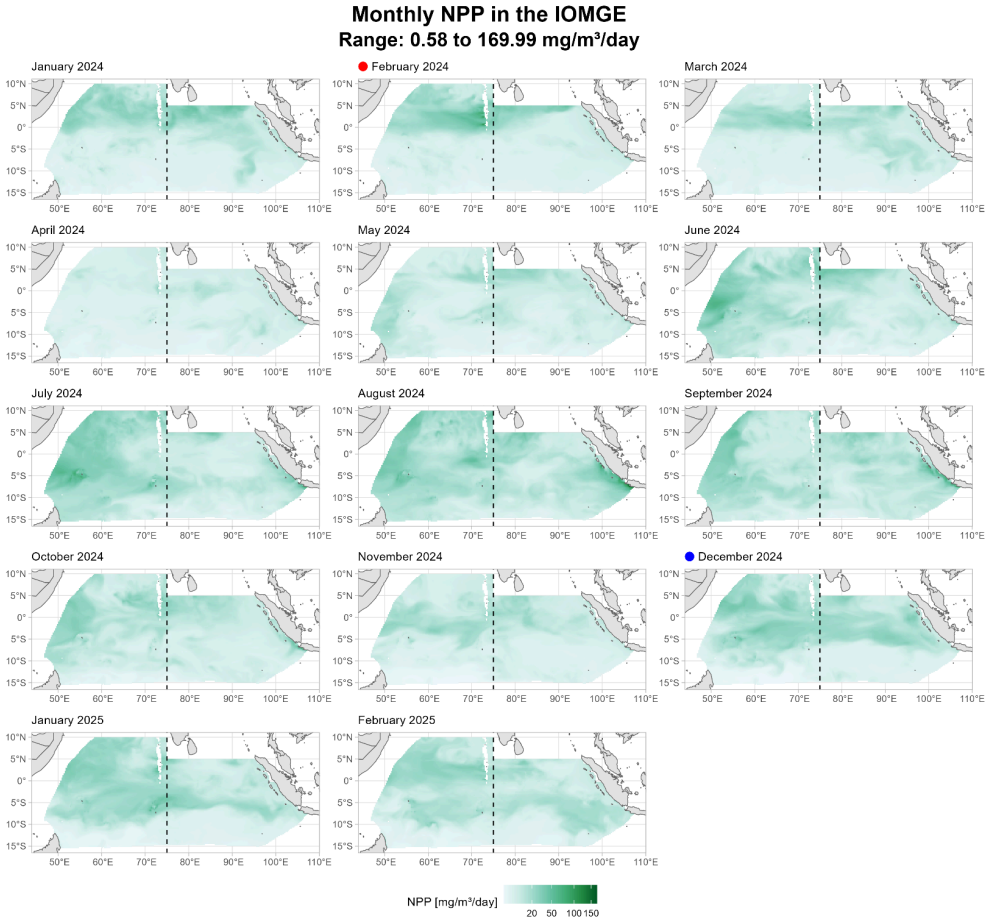

Figure 16. Monthly net primary production (NPP) in the IOMGE from January 2024 to February 2025. Dashed black line at 75°E represents the separation of the Western IOMGE and Eastern IOMGE. The red dot represents a positive Indian Ocean Dipole phase and the blue dot represents a negative Indian Ocean Dipole phase.

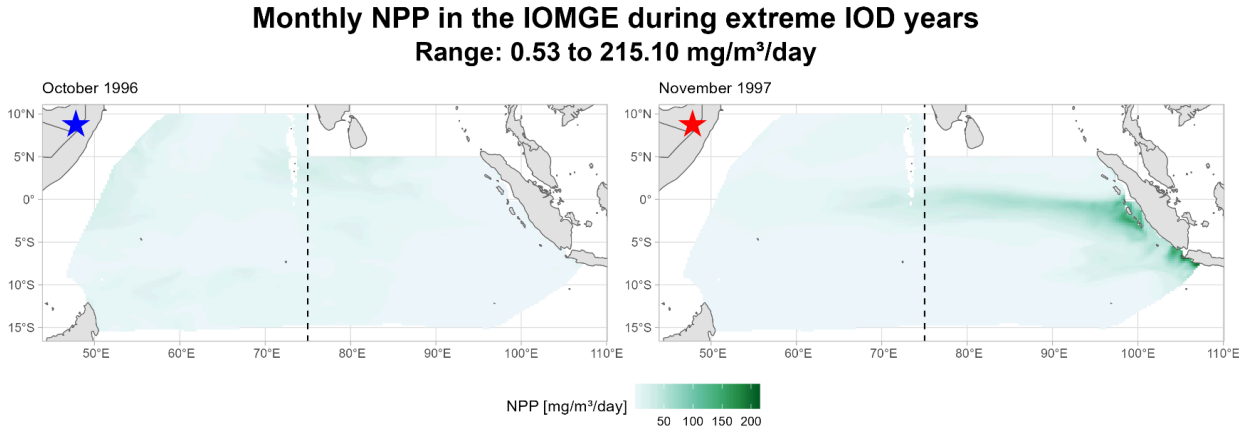

Figure 17. Spatial NPP values during extreme negative Indian Ocean Dipole year October 1996 (blue star) and during extreme positive Indian Ocean Dipole year November 1997 (red star).

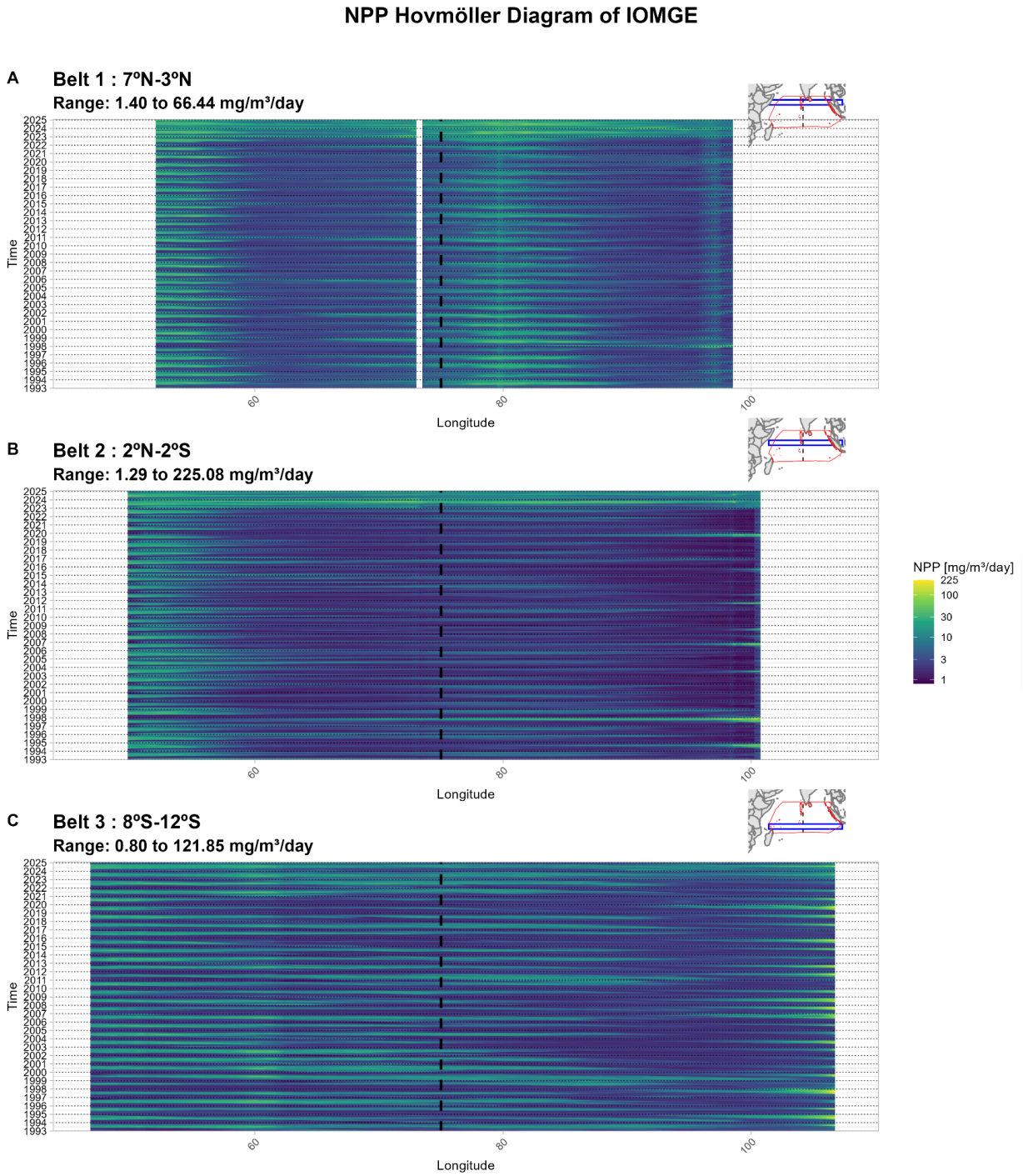

Figure 18. Hovmöller diagrams of monthly net primary production (NPP) across three latitudinal belts in the IOMGE from 1993 to 2024. Dashed line represents 75°E separating Western and Eastern IOMGE.

A)NPP values averaged over 7°N-3°N latitudinal range and varying across longitude and time. NA values represented as a gap due to Maldives land data.
B)NPP values averaged over 2°N-2°S latitudinal range and varying across longitude and time.
C)NPP values averaged over 8°S-12°S latitudinal range and varying across longitude and time.

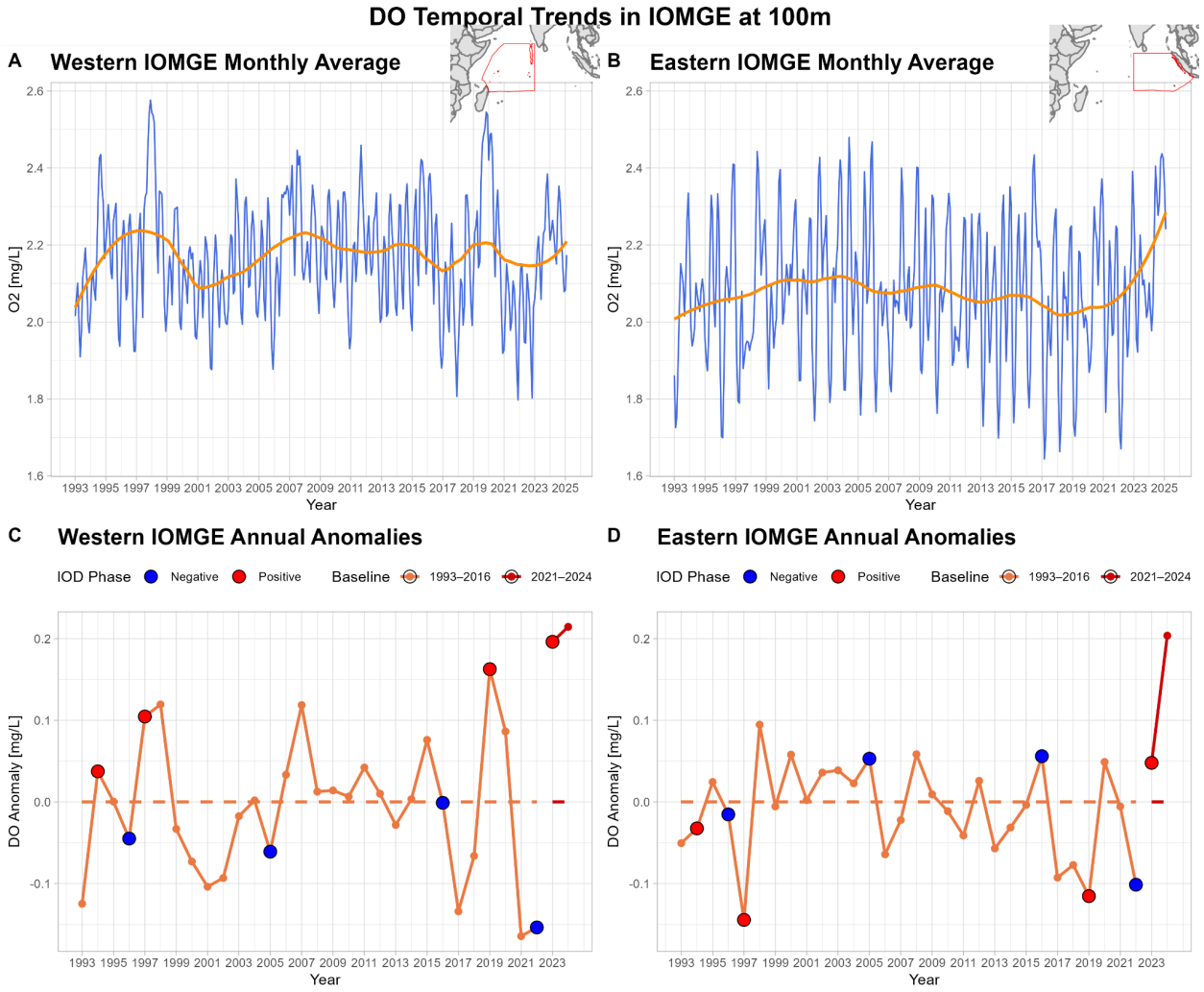

Figure 19. Time series of dissolved oxygen (DO) at 100m depth and corresponding anomalies across the IOMGE subregions (Western and Eastern IOMGE, divided at 75°E).
A) Monthly mean DO in the Western IOMGE (January 1993-February 2025).
B) Monthly mean DO in the Eastern IOMGE (January 1993-February 2025).
C) Annual DO anomalies in the Western IOMGE till 2024 (baselines: 1993-2016 & 2021-2024). Along with the addition of positive IOD years (red dots) and negative IOD years (blue dots).
D) Annual DO anomalies in the Eastern IOMGE till 2024 (baselines: 1993-2016 & 2021-2024). Along with the addition of positive IOD years (red dots) and negative IOD years (blue dots).
Note: LOESS trends are shown in orange.

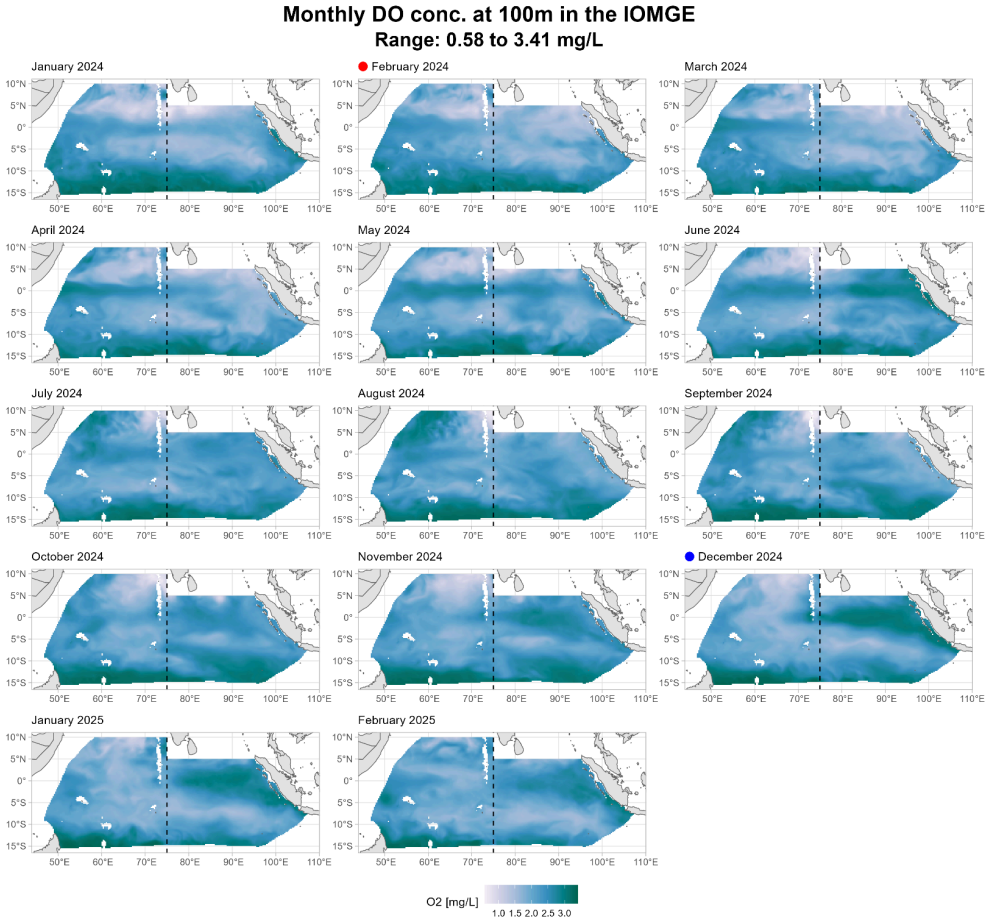

Figure 20. Monthly dissolved oxygen (DO) at 100m depth in the IOMGE from January 2024 to February 2025. Dashed black line at 75°E represents the separation of the Western IOMGE and Eastern IOMGE. The red dot represents a positive Indian Ocean Dipole phase and the blue dot represents a negative Indian Ocean Dipole phase.

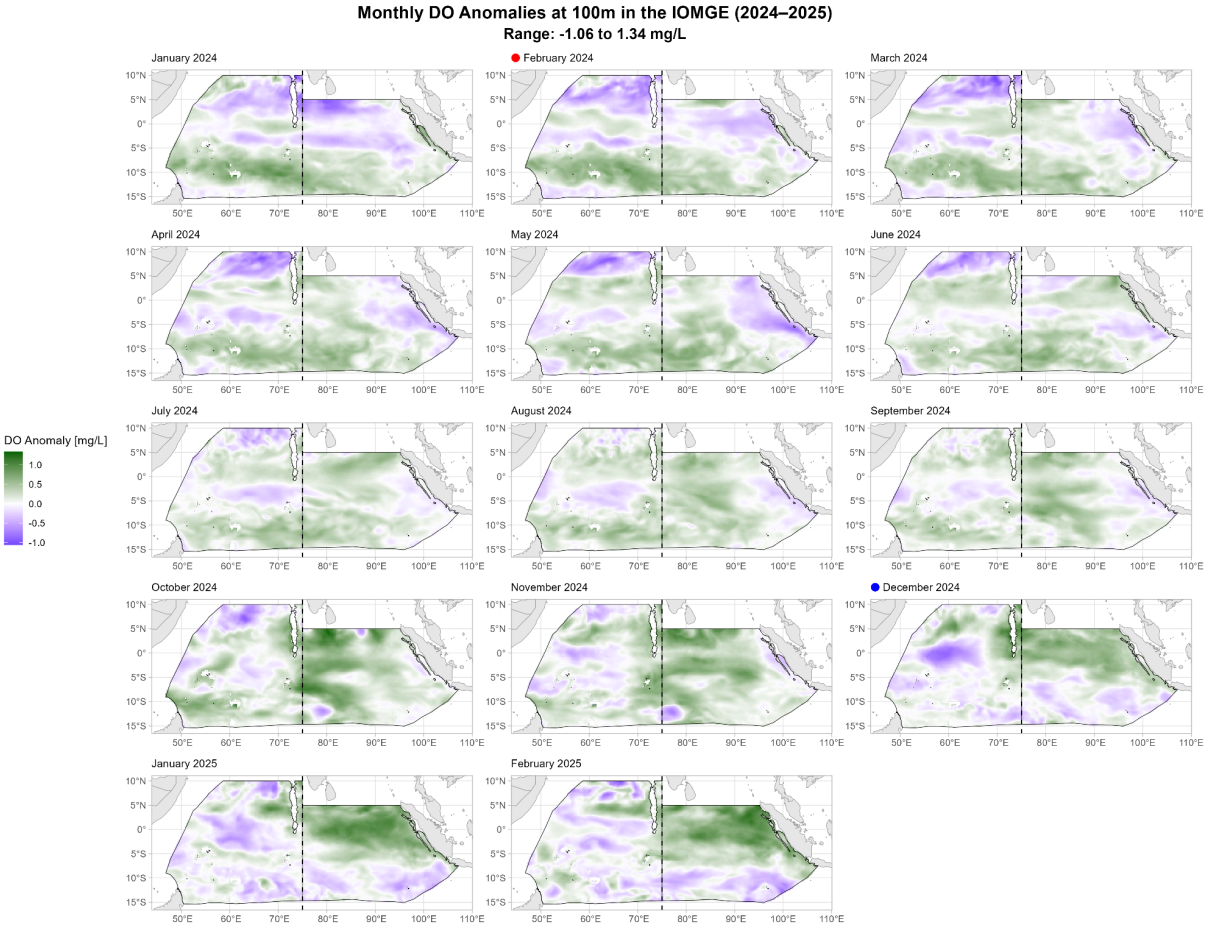

Figure 21. Monthly dissolved oxygen (DO) at 100m depth anomalies in the IOMGE from January 2024 to February 2025. Dashed black line at 75°E represents the separation of the Western IOMGE and Eastern IOMGE. The red dot represents a positive Indian Ocean Dipole phase and the blue dot represents a negative Indian Ocean Dipole phase.

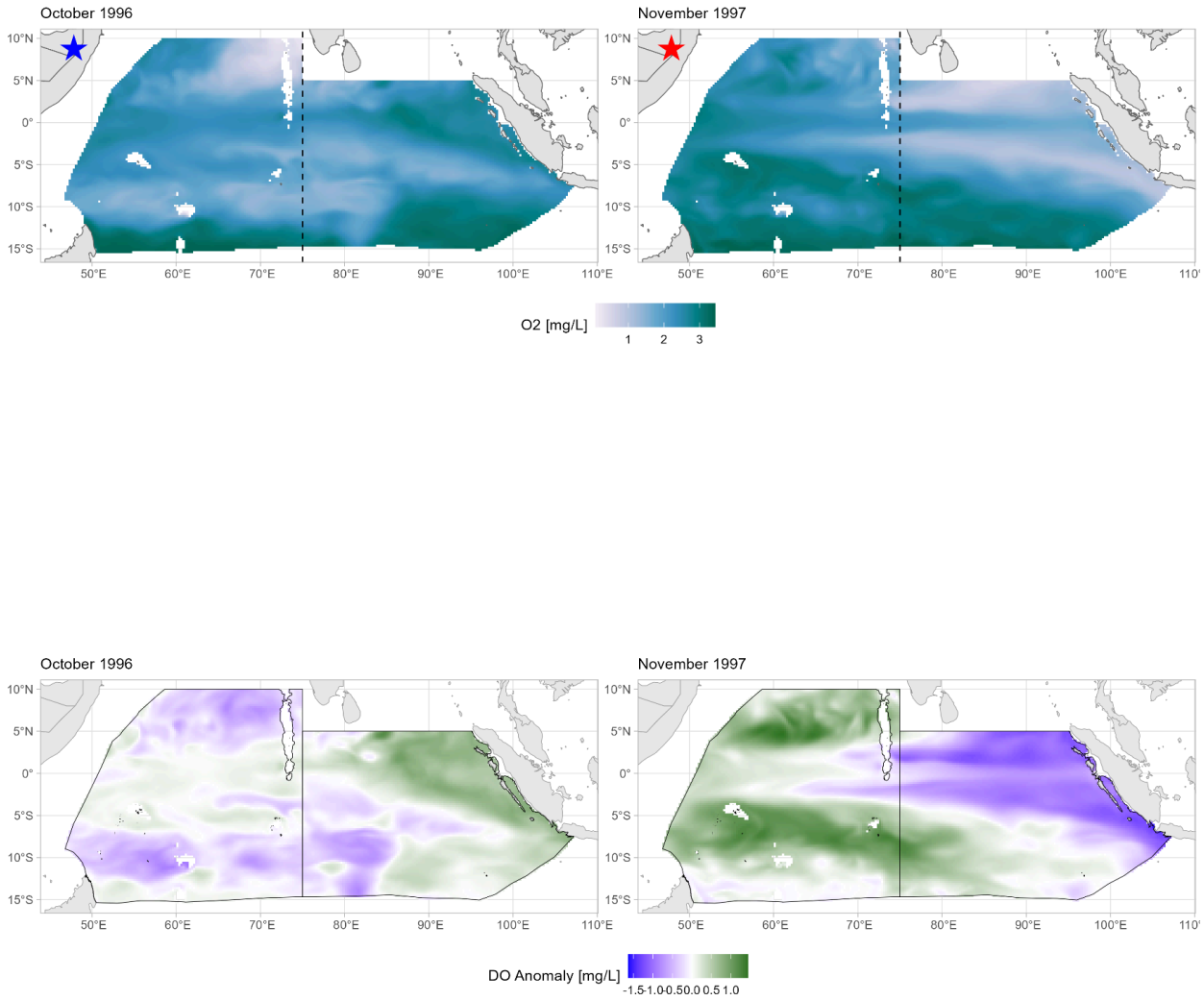

Figure 22. Spatial DO at 100m values during extreme negative Indian Ocean Dipole year October 1996 (blue star) and associated anomalies and during extreme positive Indian Ocean Dipole year November 1997 (red star) and associated anomalies.

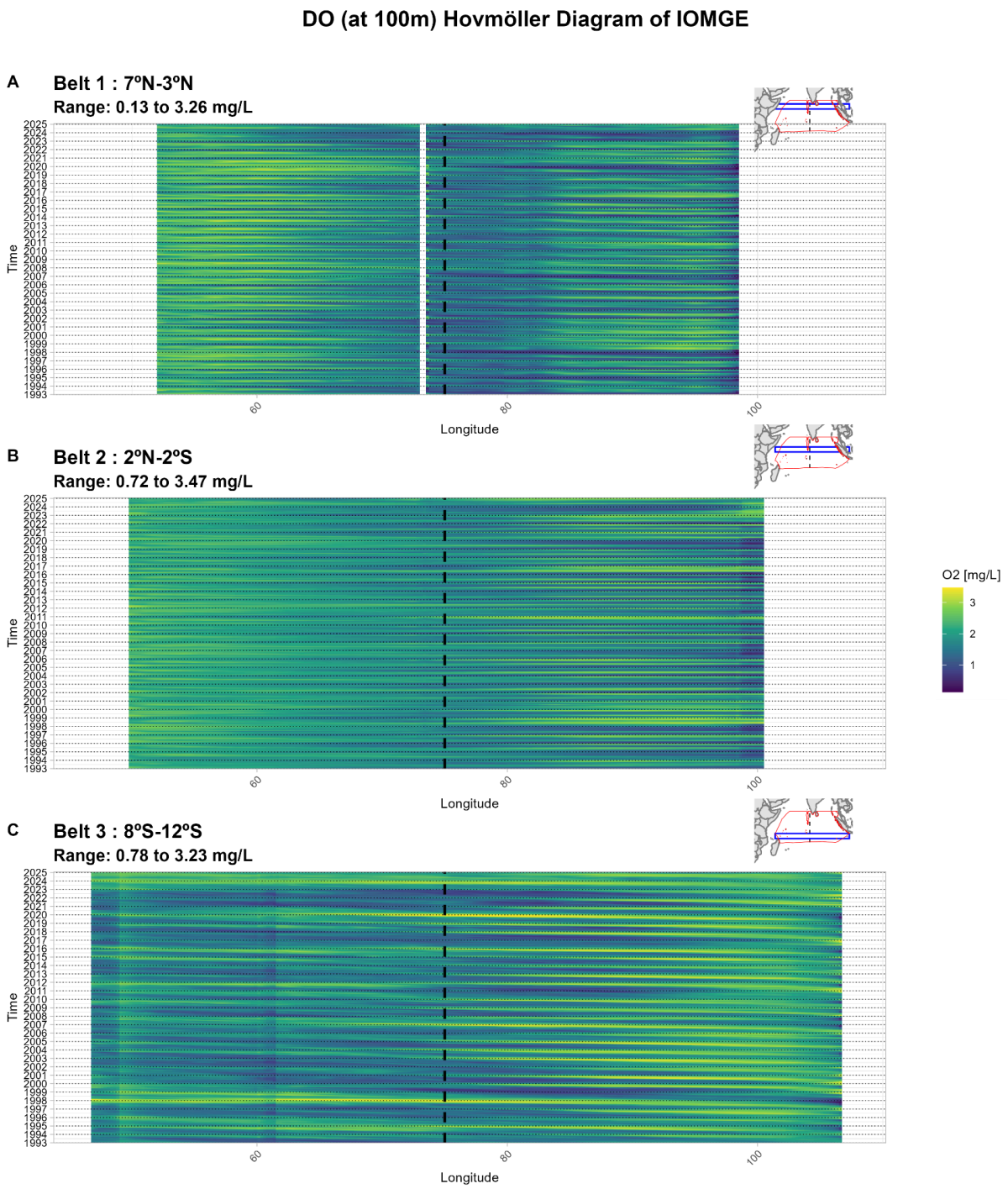

Figure 23. Hovmöller diagrams of monthly dissolved oxygen (DO) at 100m depth across three latitudinal belts in the IOMGE from 1993 to 2024. Dashed line represents 75°E separating Western and Eastern IOMGE.

A)DO values averaged over 7°N-3°N latitudinal range and varying across longitude and time. NA values represented as a gap due to Maldives land data.

B)DO values averaged over 2°N-2°S latitudinal range and varying across longitude and time.

C)DO values averaged over 8°S-12°S latitudinal range and varying across longitude and time.

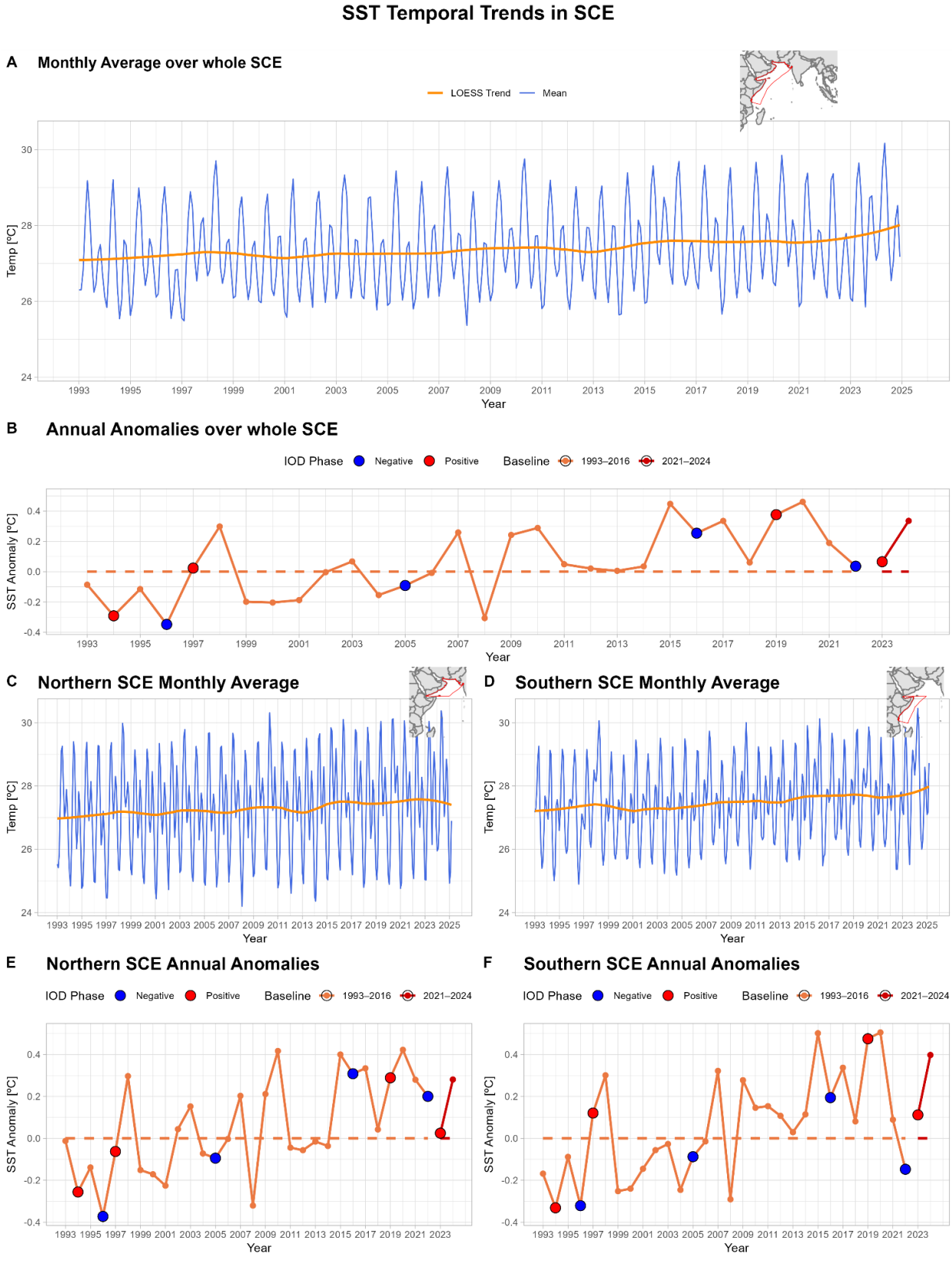
SST Temporal Trends in SCE
A
Monthly Average over whole SCE
LOESS Trend
Mean
Temp [°C]
Year
B
Annual Anomalies over whole SCE
IOD Phase
Negative
Positive
Baseline
1993–2016
2021–2024
SST Anomaly [°C]
Year
C
Northern SCE Monthly Average
D
Southern SCE Monthly Average
E
Northern SCE Annual Anomalies
F
Southern SCE Annual Anomalies

Figure 24. Temporal trends of sea surface temperature (SST) and corresponding anomalies across the SCE and its subregions (Northern and Southern SCE, divided at 12°N).
A) Monthly mean SST across the entire SCE (January 1993-March 2025).
B) Annual SST anomalies for years with complete data across the entire SCE, relative to the baselines: 1993-2016 & 2021-2024. Along with the addition of positive IOD years (red dots) and negative IOD years (blue dots).
C) Monthly mean SST in the Northern SCE (January 1993-March 2025).
D) Monthly mean SST in the Southern SCE (January 1993-March 2025).
E) Annual SST anomalies in the Northern SCE till 2024 (baselines: 1993-2016 & 2021-2024). Alongwith the addition of positive IOD years (red dots) and negative IOD years (blue dots).
F) Annual SST anomalies in the Southern SCE till 2024 (baselines: 1993-2016 & 2021-2024). Alongwith the addition of positive IOD years (red dots) and negative IOD years (blue dots).
Note: Data for June 2021 comprises just one date, i.e, 01/06/2021. LOESS trends are shown in orange.

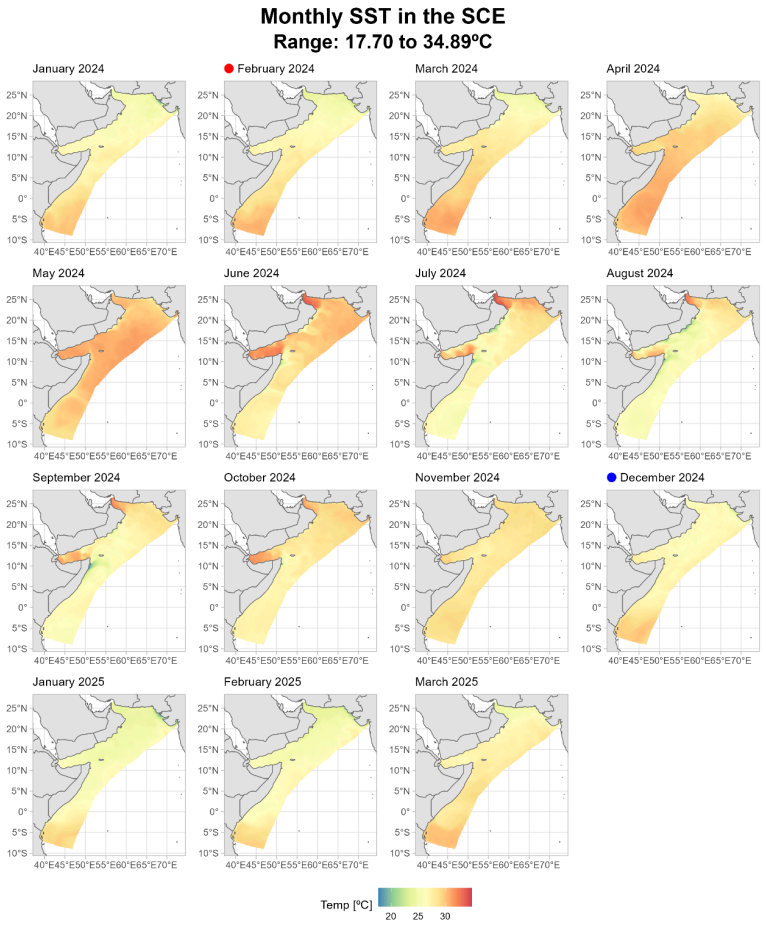

Figure 25. Monthly sea surface temperature (SST) in the SCE from January 2024 to March 2025. Dashed black line at 12°N represents the separation of the Northern SCE and Southern SCE. The red dot represents a positive Indian Ocean Dipole phase and the blue dot represents a negative Indian Ocean Dipole phase.

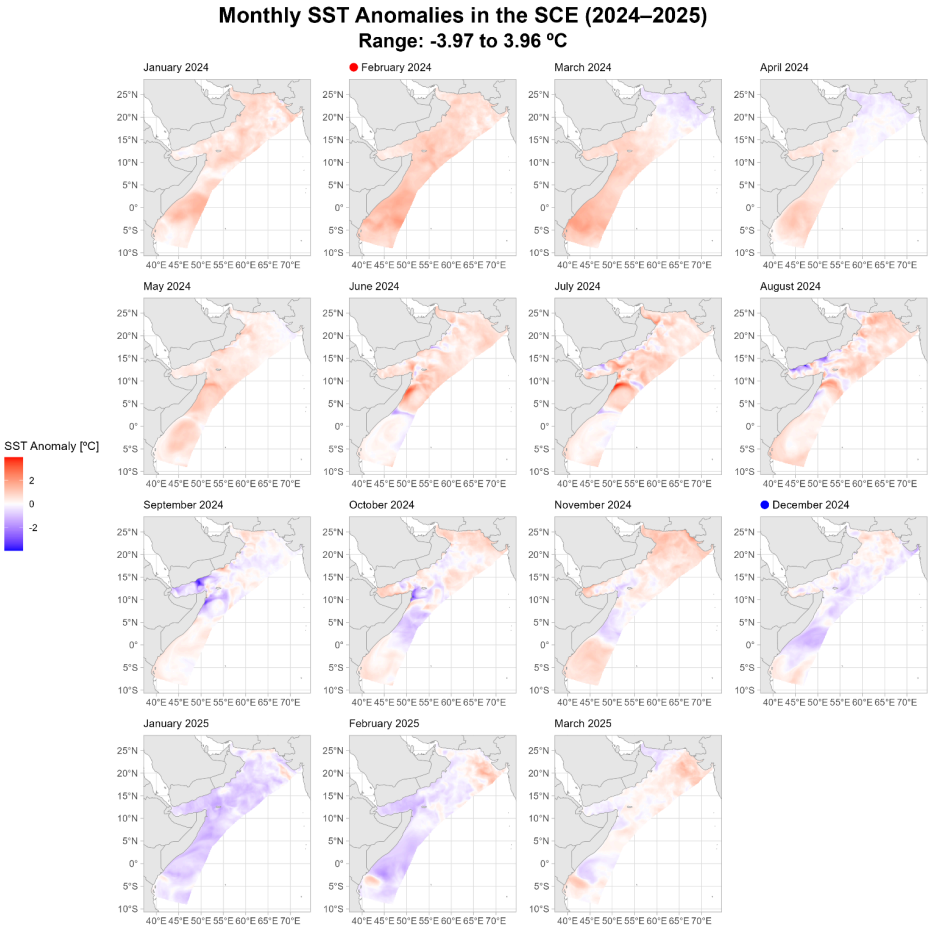

Figure 26. Monthly sea surface temperature (SST) anomalies in the SCE from January 2024 to March 2025. Dashed black line at 12°N represents the separation of the Northern SCE and Southern SCE. The red dot represents a positive Indian Ocean Dipole phase and the blue dot represents a negative Indian Ocean Dipole phase.

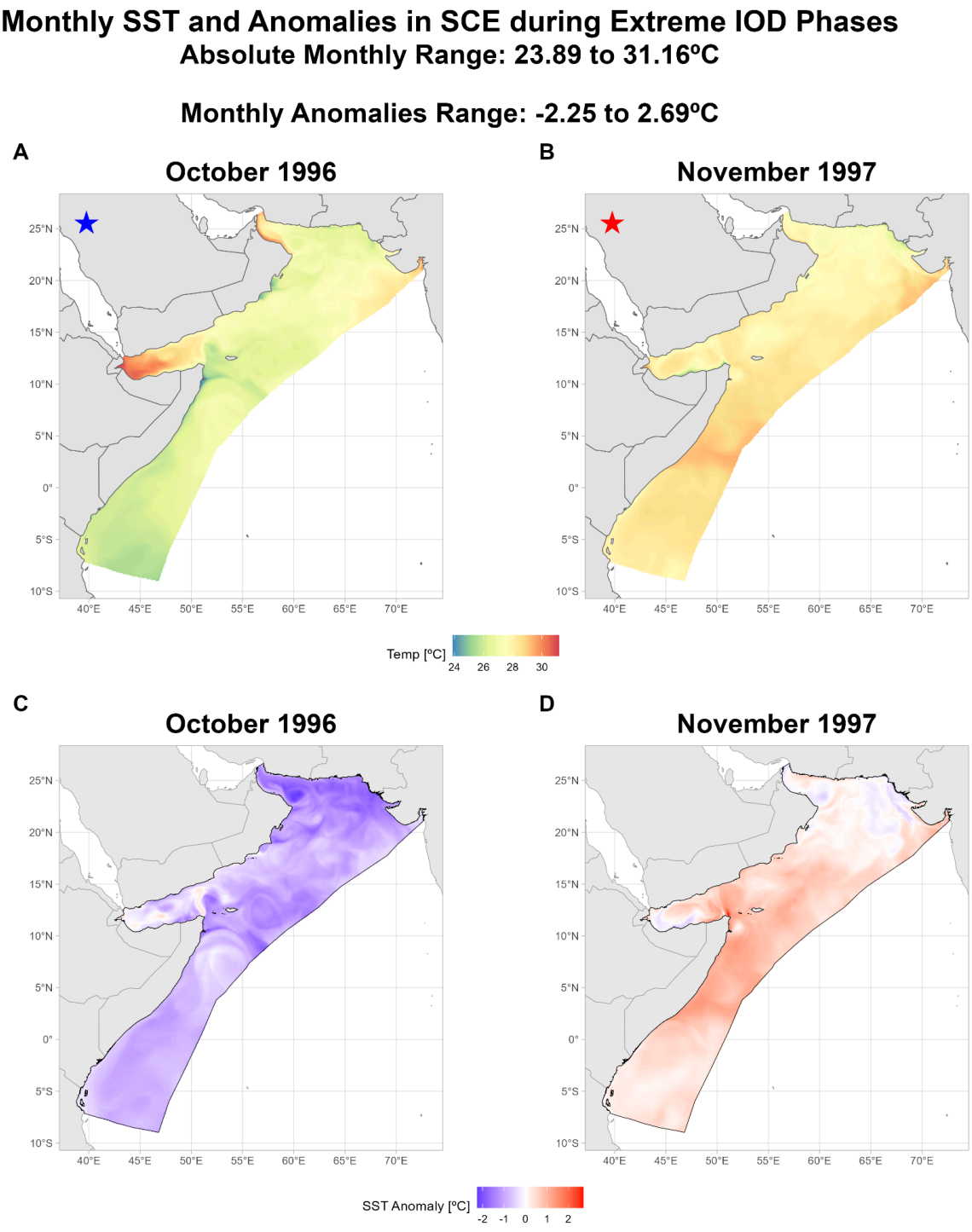

Figure 27. Spatial SST values during extreme negative Indian Ocean Dipole year October 1996 (blue star) and associated anomalies and during extreme positive Indian Ocean Dipole year November 1997 (red star) and assocaited anomalies in the SCE.

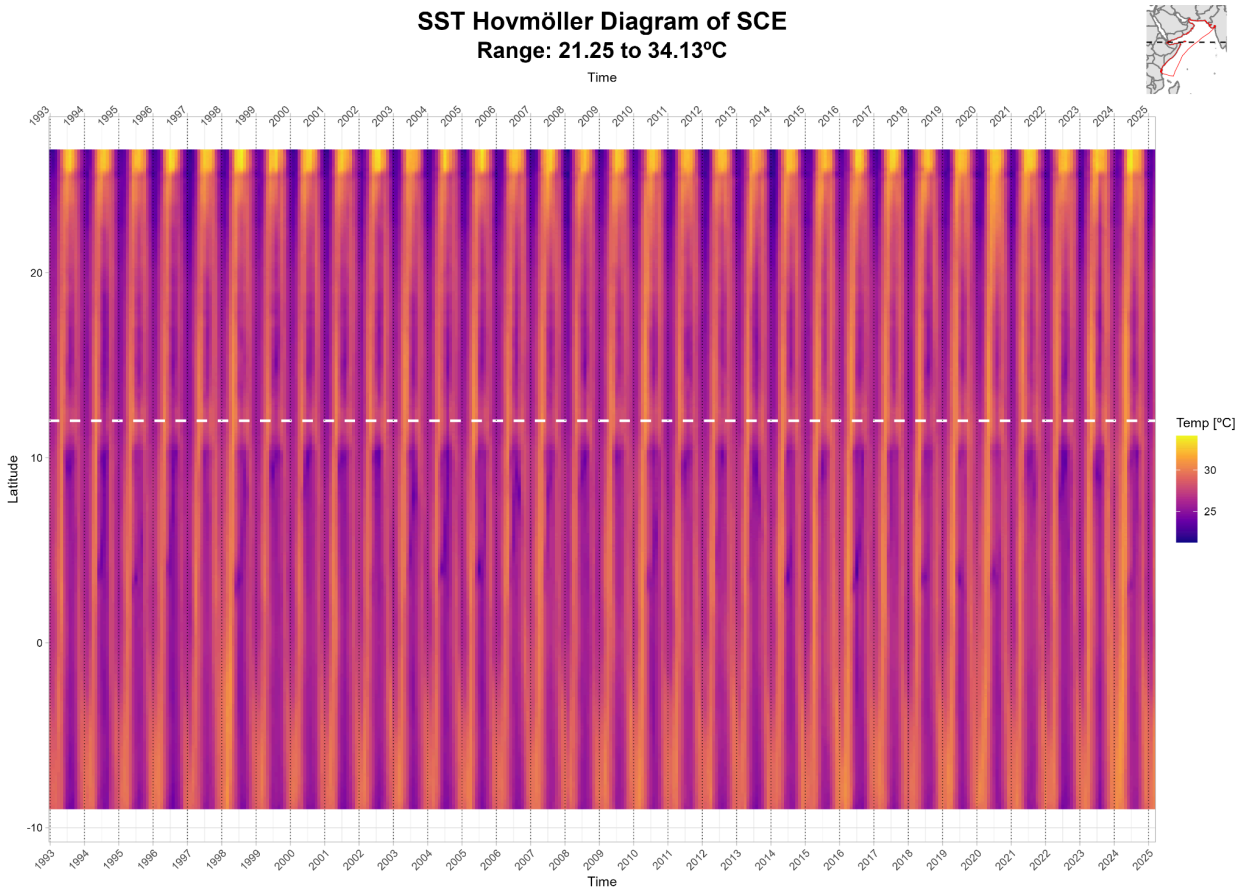

Figure 28. Hovmöller diagrams of monthly sea surface temperature (SST) across the SCE averaged across longitude and varying across latitude and time, from 1993 to 2025. Dashed line represents 12°N separating the Northern and Southern SCE.

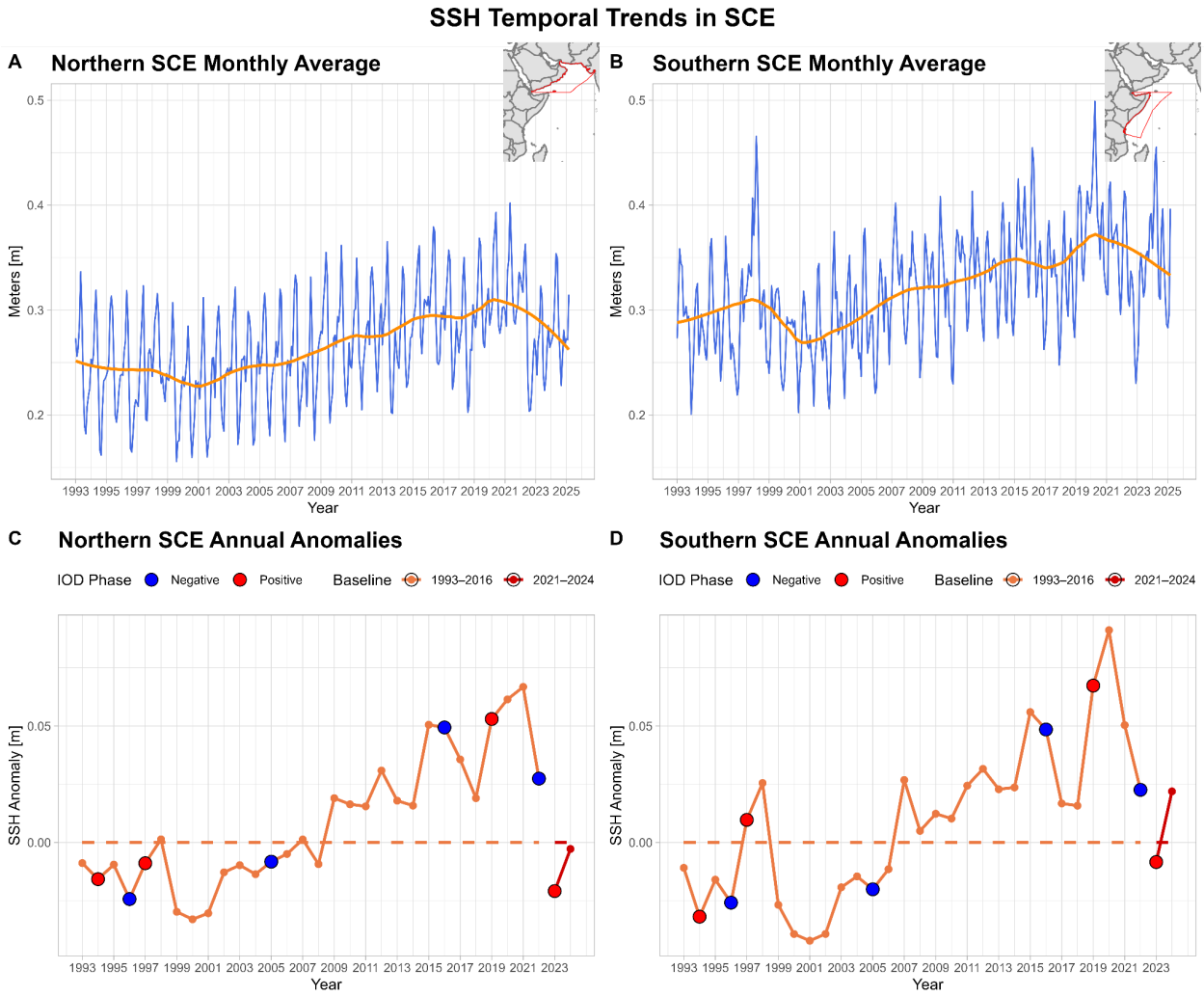

Figure 29. Time series of sea surface height (SSH) and corresponding anomalies across the SCE subregions (Northern and Southern SCE, divided at 12°N).

A) Monthly mean SSH in the Northern SCE (January 1993-March 2025).

B) Monthly mean SSH in the Southern SCE (January 1993-March 2025).

C) Annual SSH anomalies in the Northern SCE till 2024 (baselines: 1993-2016 & 2021-2024). Alongwith the addition of positive IOD years (red dots) and negative IOD years (blue dots).

D) Annual SSH anomalies in the Southern SCE till 2024 (baselines: 1993-2016 & 2021-2024). Alongwith the addition of positive IOD years (red dots) and negative IOD years (blue dots).

Note: Data for June 2021 comprises just one date, i.e, 01/06/2021. LOESS trends are shown in orange.

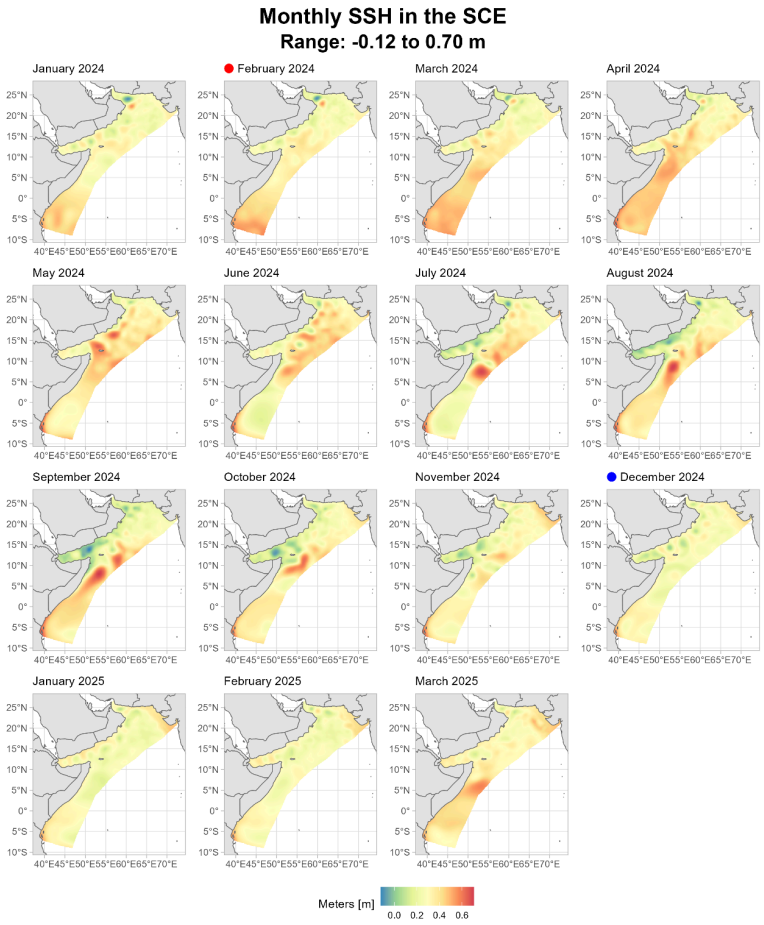

Figure 30. Monthly sea surface height (SSH) in the SCE from January 2024 to March 2025. Dashed black line at 12°N represents the separation of the Northern SCE and Southern SCE. The red dot represents a positive Indian Ocean Dipole phase and the blue dot represents a negative Indian Ocean Dipole phase.

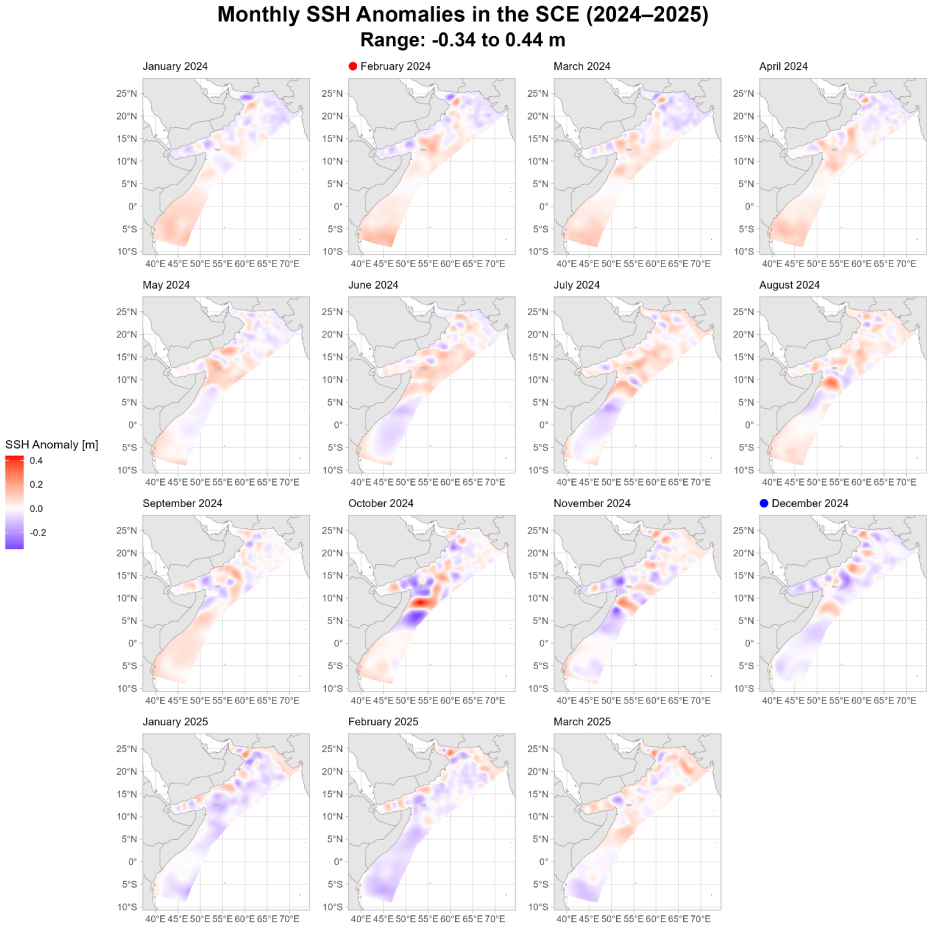

Figure 31. Monthly sea surface height (SSH) anomalies in the SCE from January 2024 to March 2025. Dashed black line at 12°N represents the separation of the Northern SCE and Southern SCE. The red dot represents a positive Indian Ocean Dipole phase and the blue dot represents a negative Indian Ocean Dipole phase.

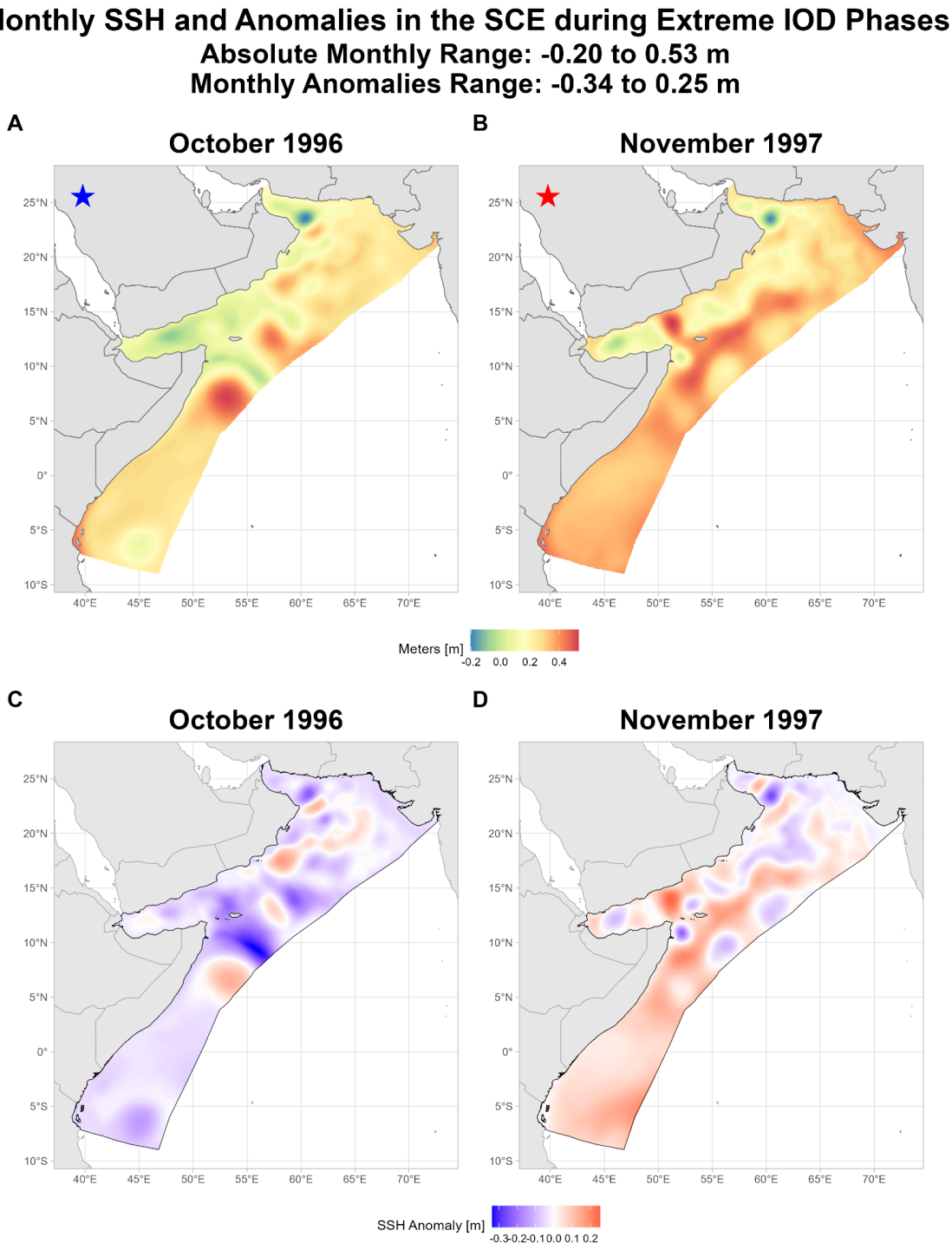

Figure 32. Spatial SSH values during extreme negative Indian Ocean Dipole year October 1996 (blue star) and associated anomalies and during extreme positive Indian Ocean Dipole year November 1997 (red star) and associated anomalies in the SCE.

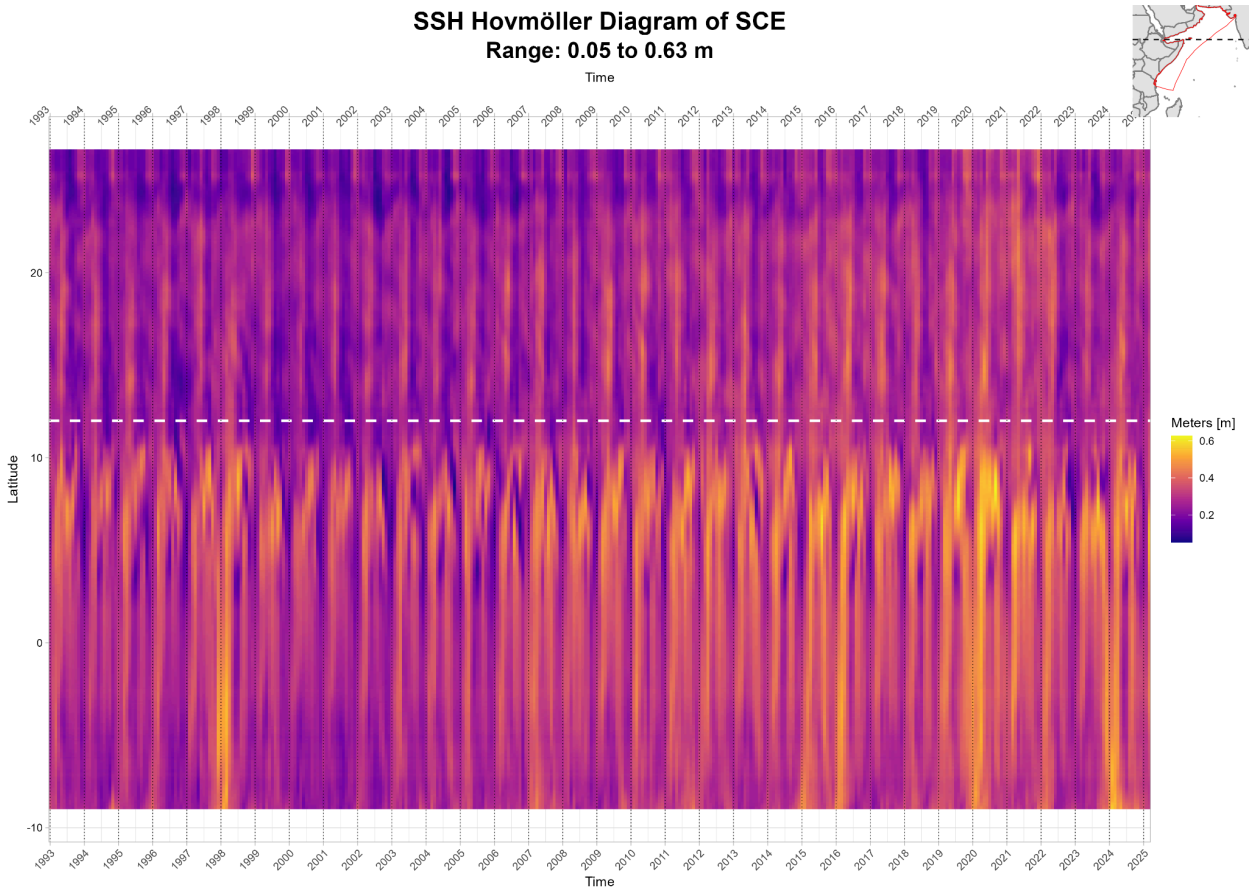

Figure 33. Hovmöller diagrams of monthly sea surface height (SSH) across the SCE averaged across longitude and varying across latitude and time, from 1993 to 2025. Dashed line represents 12°N separating the Northern and Southern SCE.

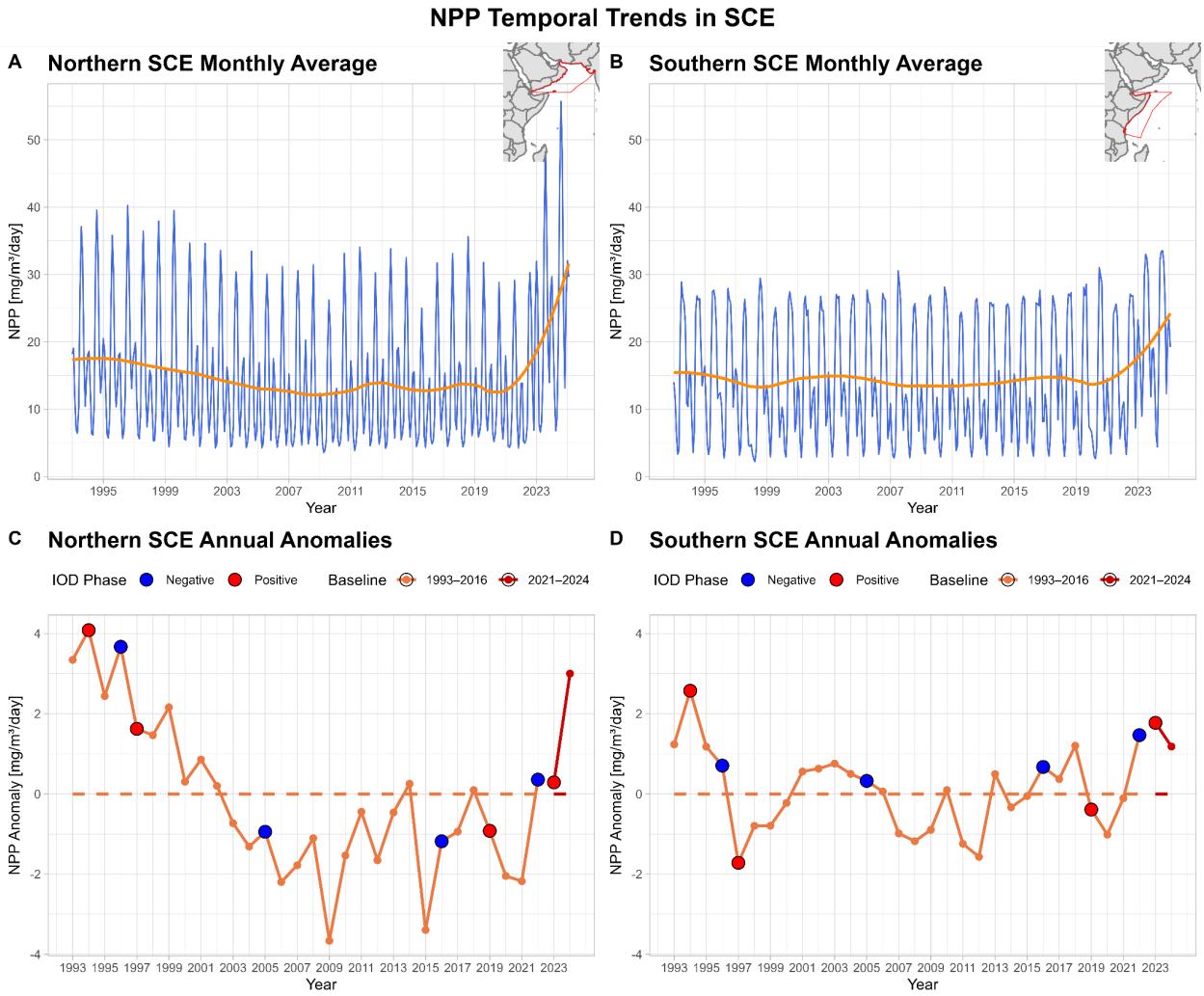

Figure 34. Time series of net primary production (NPP) and corresponding anomalies across the SCE subregions (Northern and Southern SCE, divided at 12°N).

A) Monthly mean NPP in the Northern SCE (January 1993-February 2025).

B) Monthly mean NPP in the Southern SCE (January 1993-February 2025).

C) Annual NPP anomalies in the Northern SCE till 2024 (baselines: 1993-2016 & 2021-2024). Alongwith the addition of positive IOD years (red dots) and negative IOD years (blue dots).

D) Annual NPP anomalies in the Southern SCE till 2024 (baselines: 1993-2016 & 2021-2024). Alongwith the addition of positive IOD years (red dots) and negative IOD years (blue dots).

Note: LOESS trends are shown in orange.

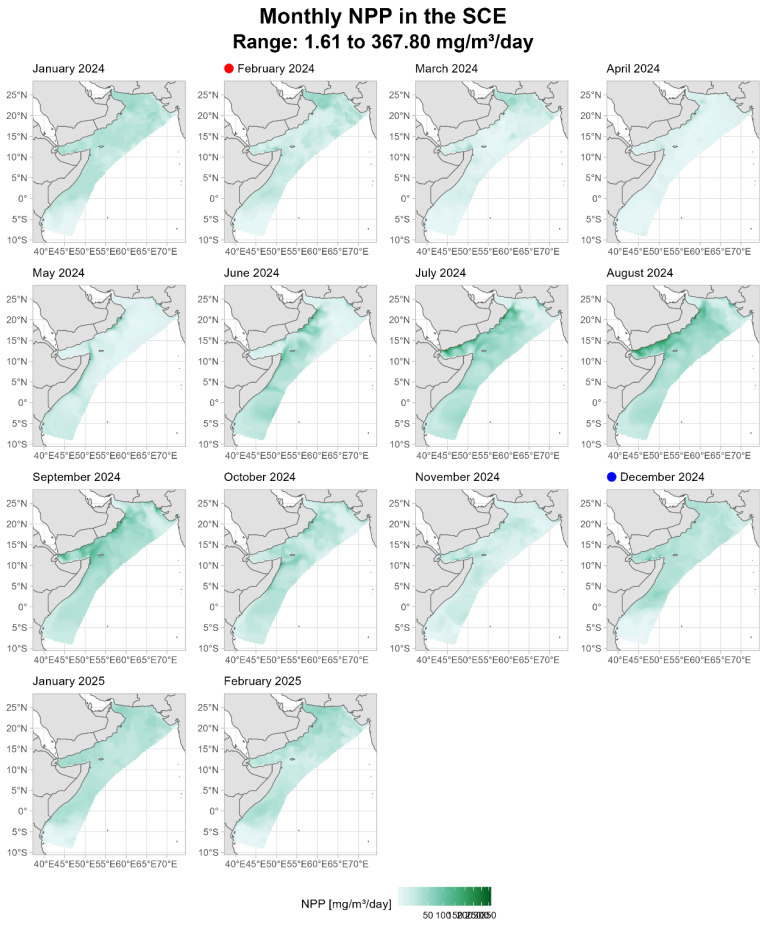

Figure 35. Monthly net primary production (NPP) in the SCE from January 2024 to February 2025. Dashed black line at 12°N represents the separation of the Northern SCE and Southern SCE. The red dot represents a positive Indian Ocean Dipole phase and the blue dot represents a negative Indian Ocean Dipole phase.

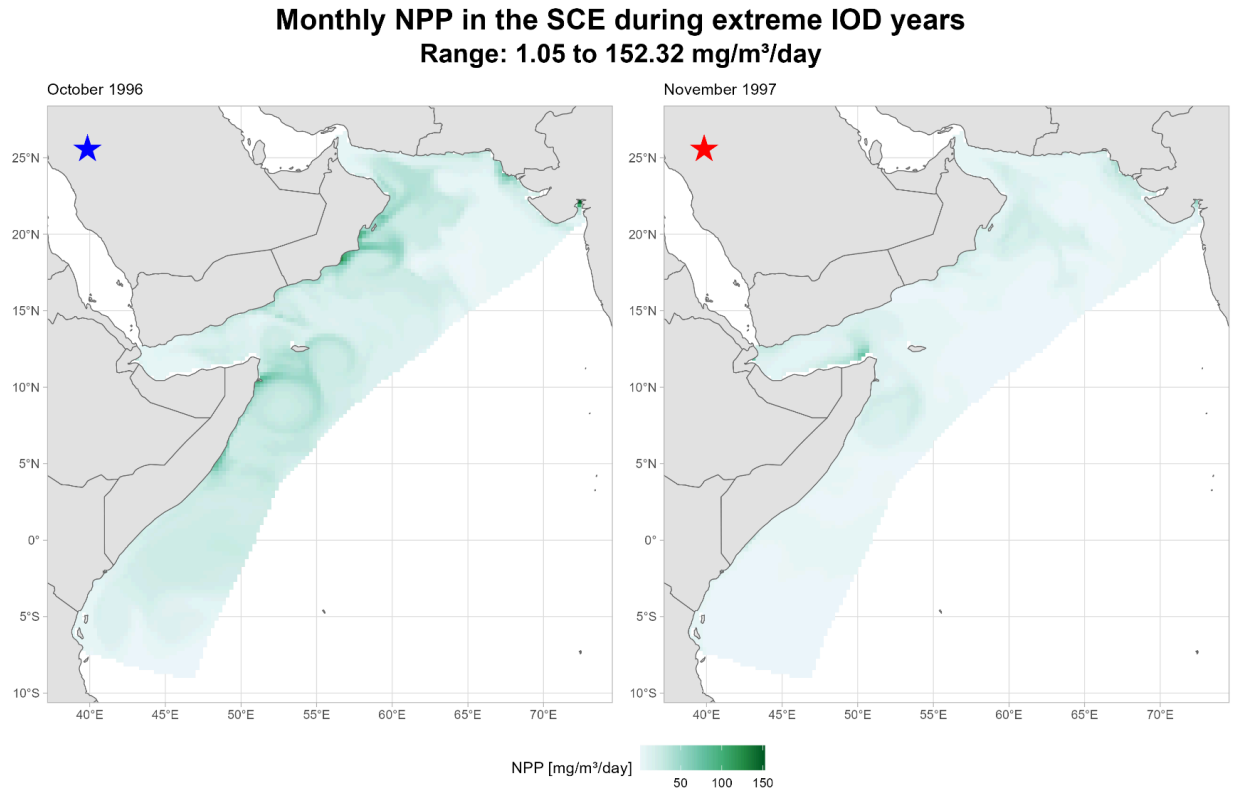

Figure 36. Spatial NPP values during extreme negative Indian Ocean Dipole year October 1996 (blue star) and during extreme positive Indian Ocean Dipole year November 1997 (red star).

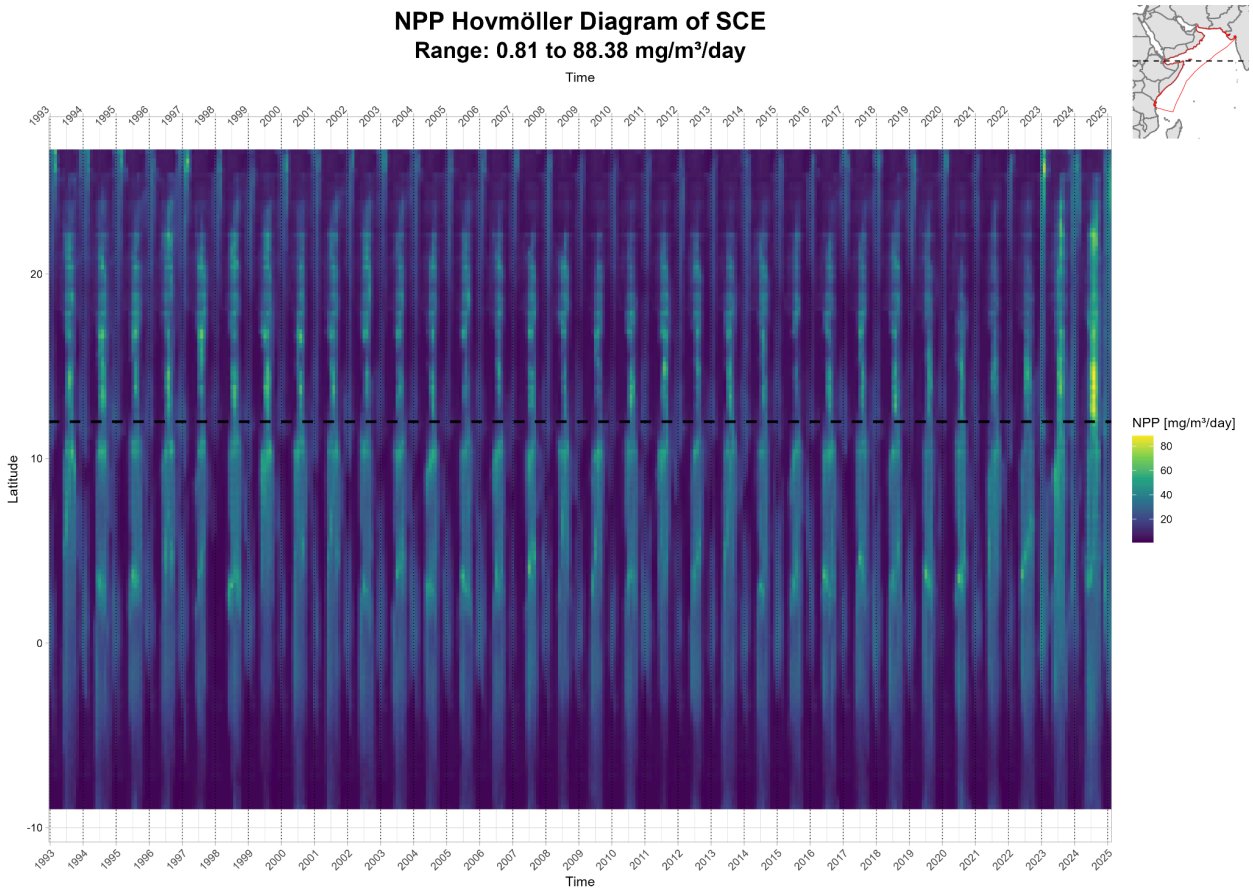

Figure 37. Hovmöller diagrams of monthly net primary production (NPP) across the SCE averaged across longitude and varying across latitude and time, from January 1993 to February 2025. Dashed line represents 12°N separating the Northern and Southern SCE.

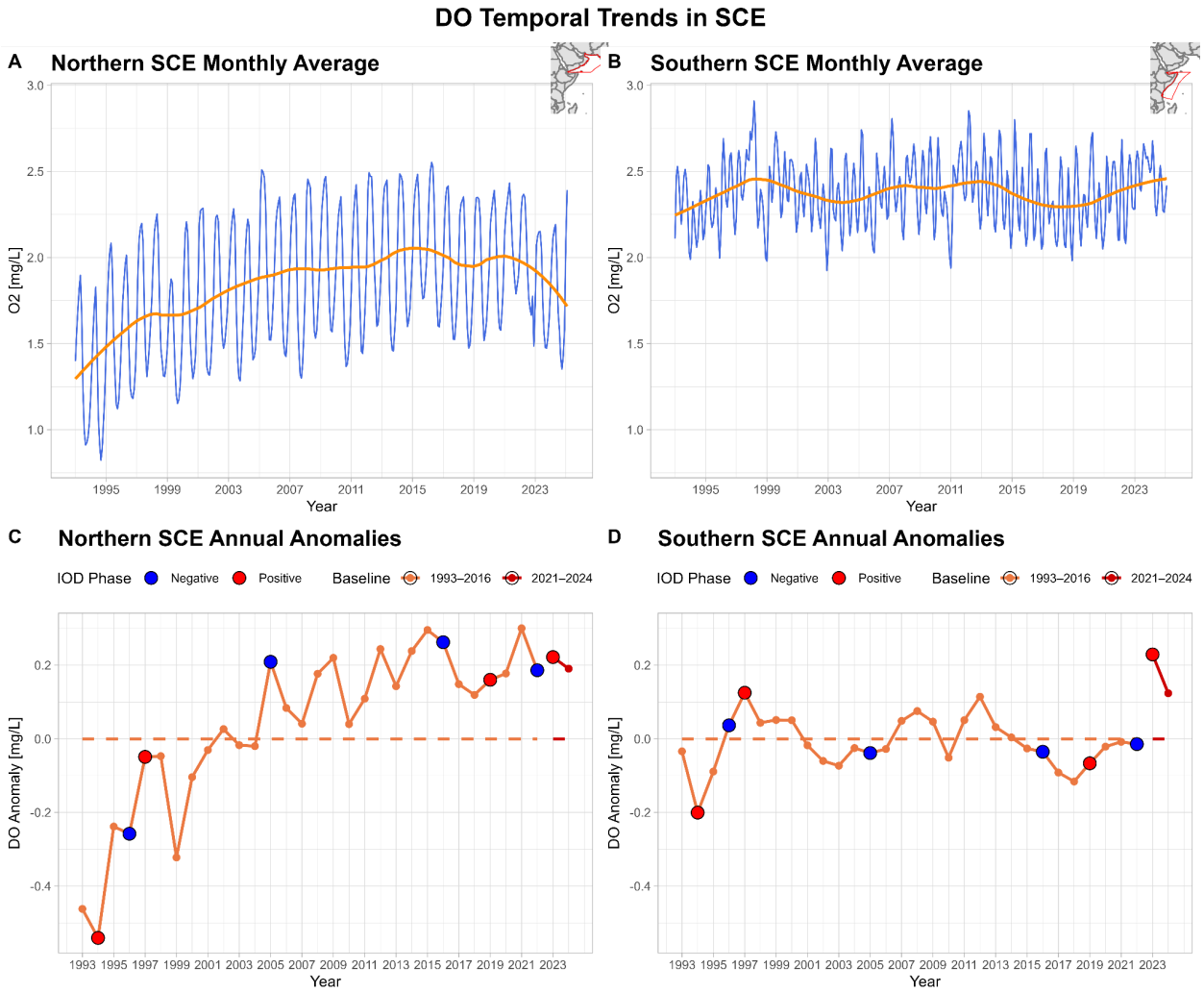

Figure 38. Time series of dissolved oxygen (DO) at 100m depth and corresponding anomalies across the SCE subregions (Northern and Southern SCE, divided at 12°N).

A) Monthly mean DO in the Northern SCE (January 1993-February 2025).

B) Monthly mean DO in the Southern SCE (January 1993-February 2025).

C) Annual DO anomalies in the Northern SCE till 2024 (baselines: 1993-2016 & 2021-2024). Alongwith the addition of positive IOD years (red dots) and negative IOD years (blue dots).

D) Annual DO anomalies in the Southern SCE till 2024 (baselines: 1993-2016 & 2021-2024). Alongwith the addition of positive IOD years (red dots) and negative IOD years (blue dots).

Note: LOESS trends are shown in orange.

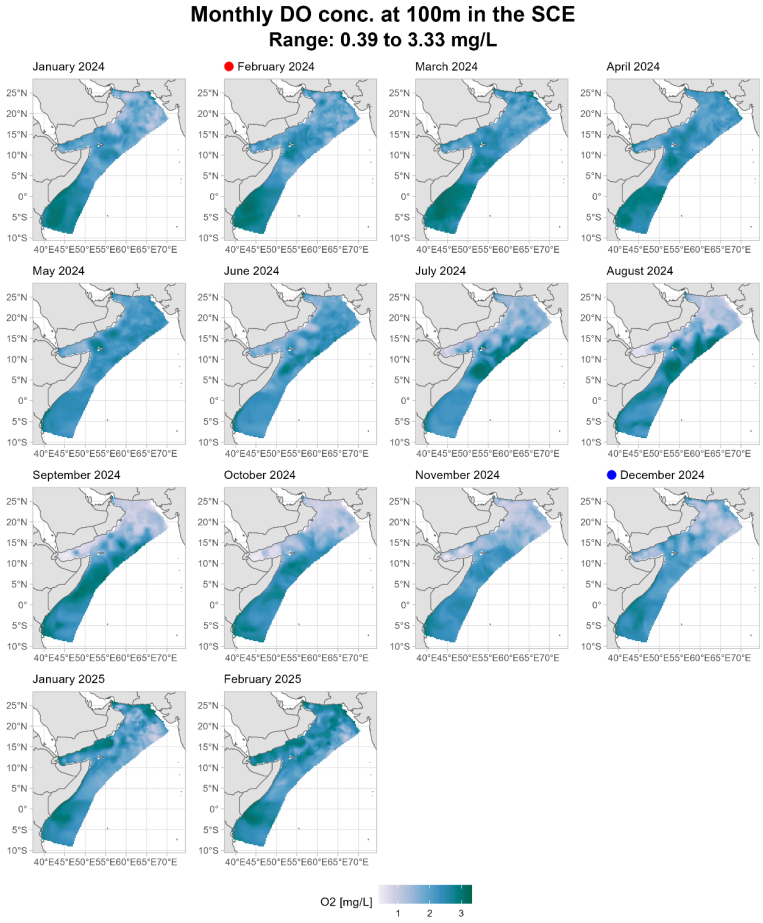

Figure 39. Monthly dissolved oxygen (DO) at 100m depth in the SCE from January 2024 to February 2025. Dashed black line at 12°N represents the separation of the Northern SCE and Southern SCE. The red dot represents a positive Indian Ocean Dipole phase and the blue dot represents a negative Indian Ocean Dipole phase.

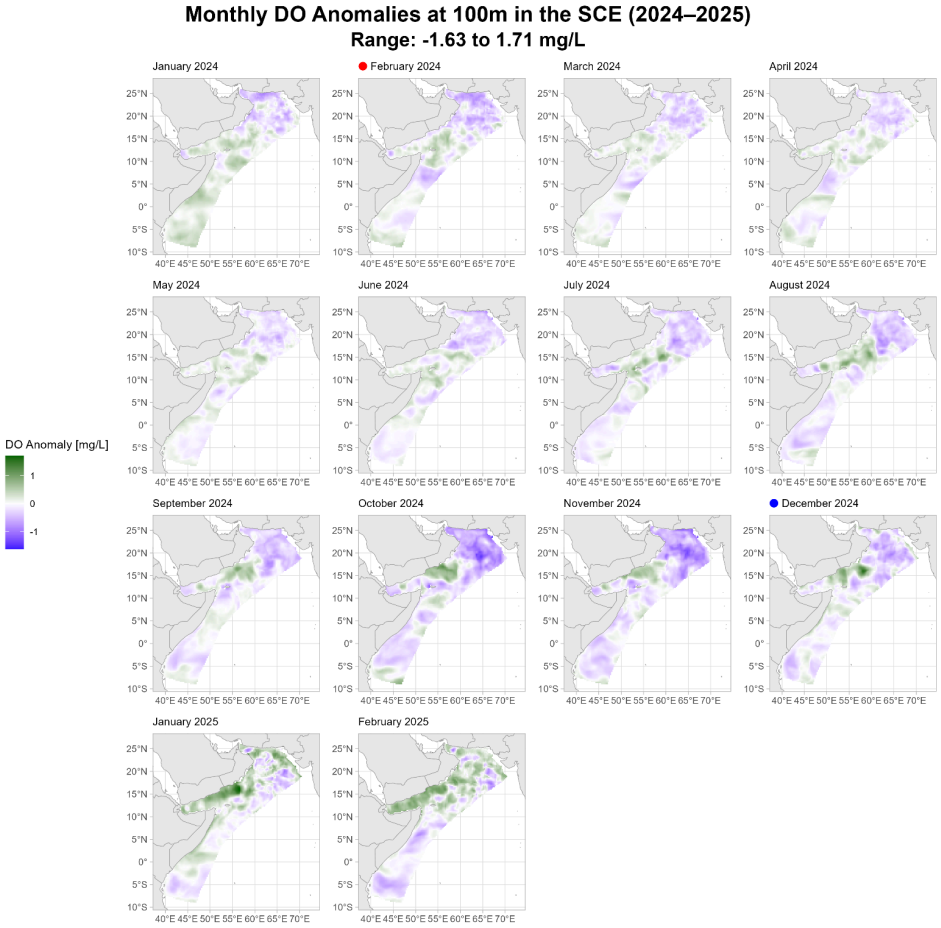

Figure 40. Monthly dissolved oxygen (DO) at 100m depth anomalies in the SCE from January 2024 to February 2025. Dashed black line at 12°N represents the separation of the Northern SCE and Southern SCE. The red dot represents a positive Indian Ocean Dipole phase and the blue dot represents a negative Indian Ocean Dipole phase.

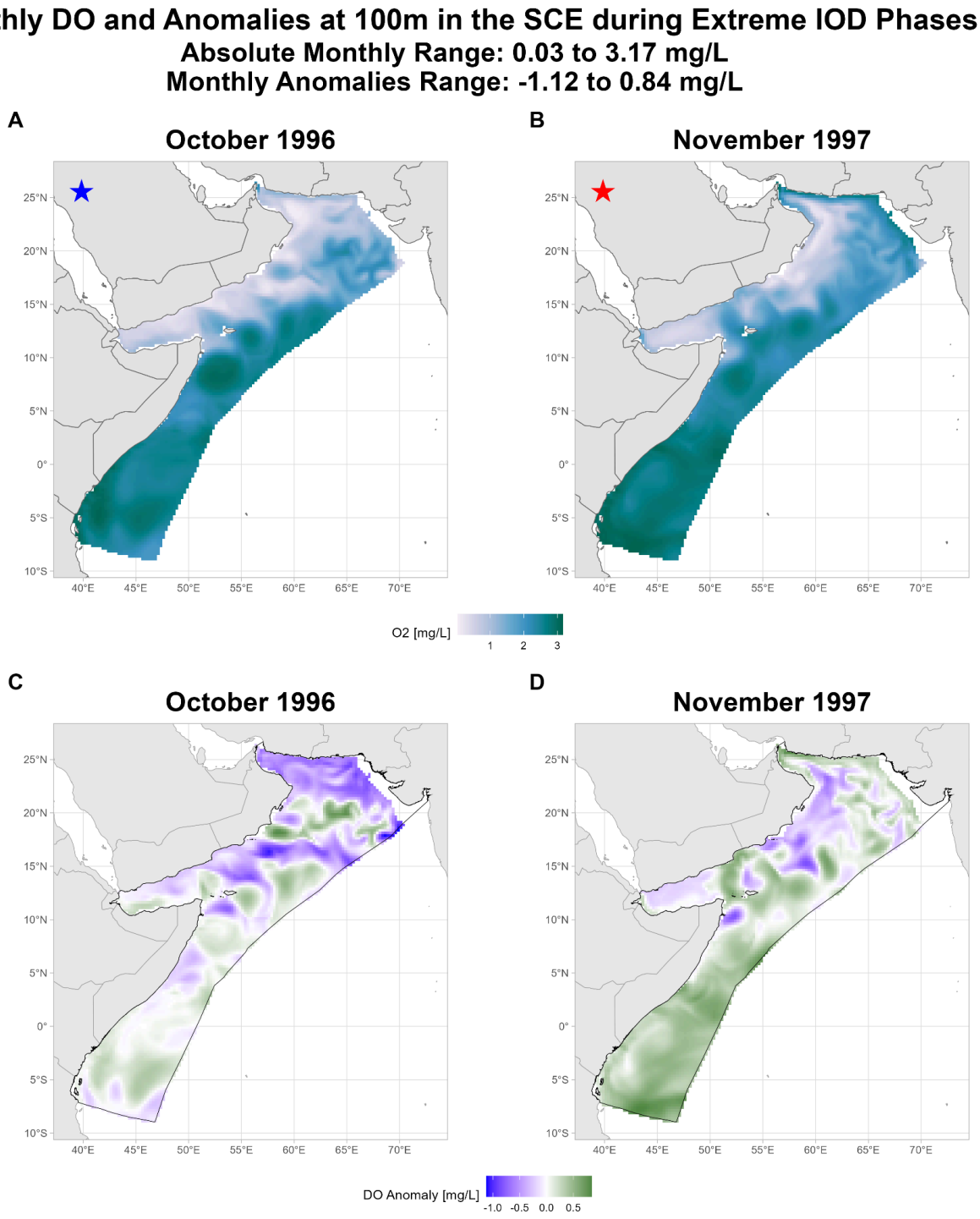

Figure 41. Spatial DO values at 100m during extreme negative Indian Ocean Dipole year October 1996 (blue star) and associated anomalies and during extreme positive Indian Ocean Dipole year November 1997 (red star) and associated anomalies in the SCE.

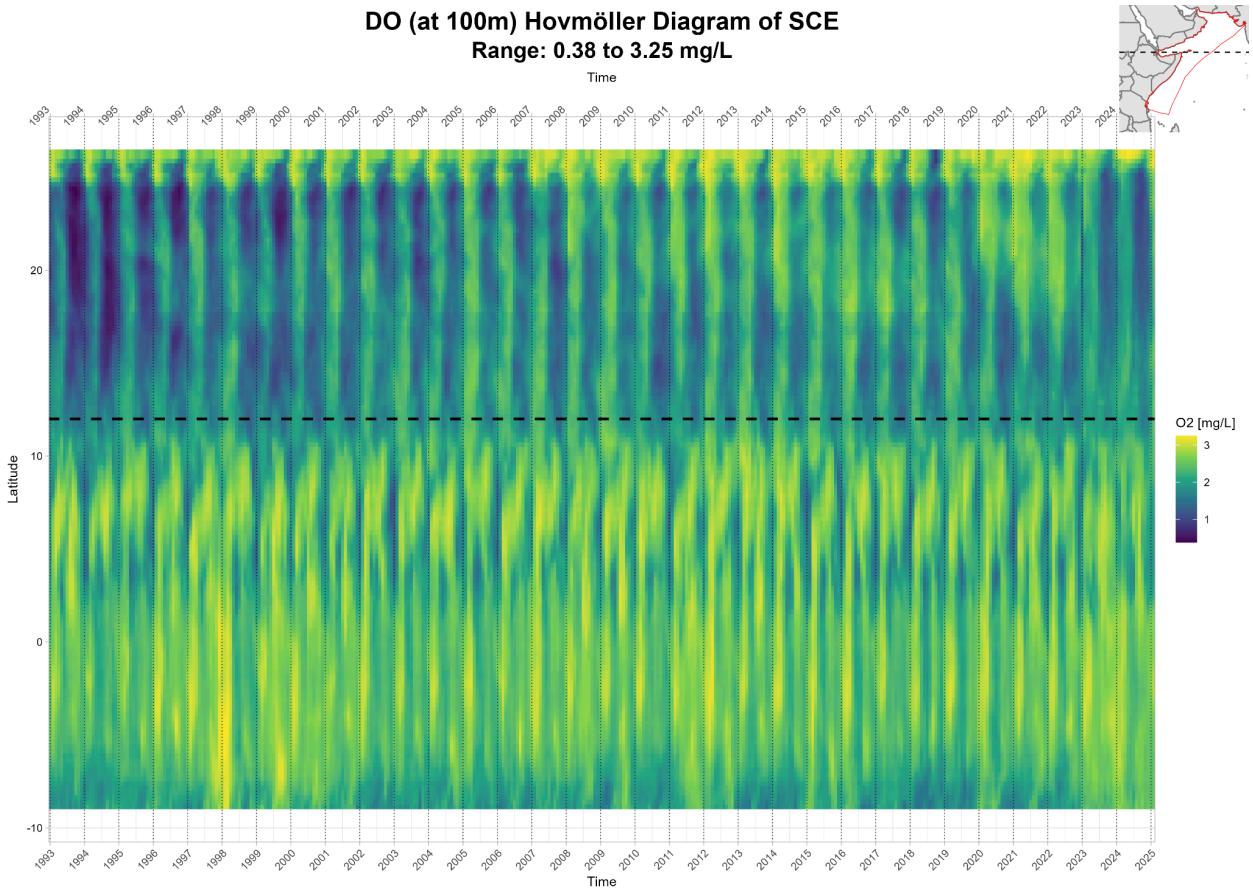

Figure 42. Hovmöller diagrams of monthly dissolved oxygen (DO) at 100m depth across the SCE averaged across longitude and varying across latitude and time, from January 1993 to February 2025. Dashed line represents 12°N separating Northern and Southern SCE.